# In-depth resolution of the magneto-optical Kerr effect in ferromagnetic multilayers

J. Hamrle*
*Laboratoire de Physique des Solides, UMR CNRS 8502, Université Paris-XI, F-91405 Orsay, France*
*and Institute of Physics, Charles University, Ke Karlovu 3, CZ-121 16, Praha 2, Czech Republic*

J. Ferré
*Laboratoire de Physique des Solides, UMR CNRS 8502, Université Paris-XI, F-91405 Orsay, France*

M. Nývlt† and Š. Višňovský
*Institute of Physics, Charles University, Ke Karlovu 3, CZ-121 16, Praha 2, Czech Republic*
(Received 14 July 2002; published 31 December 2002)

How does one determine the magnetization state and hysteresis loop corresponding to one of the ferromagnetic (FM) layers located at a given depth in a stack of FM/non-FM layers by means of the magneto-optical Kerr effect? For this purpose the representation of the Kerr effect in the complex rotation-ellipticity plane is introduced. A depth sensitivity function controlling the Kerr effect is defined and its dependence on the photon energy and angle of incidence is studied. A general way to determine the in-depth location of the FM layer, from which the Kerr signal originates, is proposed. In the case of a FM bilayer structure, previous proposed solutions are discussed within a unified formalism. For a system with three or more FM layers two approaches are proposed to extract selectively the magneto-optical signals originating at individual FM layers: the parallel Kerr vector and cascade numerical projection methods. These methods are successively checked experimentally on simple multilayer structures. Finally, on the basis of the developed approaches a readout solution for multivalued magneto-optical recording in a four-storage-layer structure is proposed.

DOI: 10.1103/PhysRevB.66.224423 PACS number(s): 75.70.−i, 75.75.+a, 78.20.Ls

## INTRODUCTION

The purpose of this paper is to understand basic principles of the in-depth sensitivity of the magneto-optical Kerr effect (later called the ''Kerr effect'') to check selective magnetization in stratified structures composed of several ultrathin ferromagnetic (FM) layers separated by nonferromagnetic (nFM) spacers. This approach can be used to obtain a better understanding of the magnetic behavior of ultrathin film structures, for example those used in engineering devices based on giant and tunnel magnetoresistances.

The Kerr effect has been widely used to solve fundamental problems in thin FM layers or to study magnetization reversal and anisotropy in a single FM layer or magnetic interactions in exchange coupled FM bilayers.[1–4] Although the in-depth dependence of the Kerr effect was treated both analytically and numerically,[5,6] the problem of the separation of Kerr effect contributions coming from several FM layers located at a fixed depth has not been addressed so far. Up to now, this problem has been only solved for systems involving two ultrathin FM layers, separated by a non-FM spacer layer. In this case the magnetization behavior of each FM layer can be probed independently by the Kerr effect by changing either the photon energy,[7] the angle of incidence,[8] or the polarization state of the incident light beam.[4,9] This last method has been elegantly used through its microscopy mode to demonstrate unambiguously the presence of a biquadratic exchange coupling between Fe layers in the Fe/Cr/Fe structure for selected Cr thicknesses.[4] It is of course useful to obtain information about the magnetic state of each FM layer in a multilayer structure consisting of more than two FM layers. In this paper procedures are proposed to solve this problem.

Only a few techniques are able to probe the magnetization state of buried FM layers. Polarized neutron reflectometry allowed one to evidence chiral spin structures in several types of exchange FM layers with competing anisotropies,[10] but the in-depth resolution there is still too low to investigate ultrathin film structures. X-ray resonant magnetic reflectometry performed at variable incidence is a very promising technique for determining an in-depth profile of the magnetization.[11] X-ray photoemission electron microscopy was used successfully to image both the Co and $LaFeO_3$ magnetic domain structures of a $Co(1.2\ nm)/LaFeO_3$ sample.[12] It has been also shown that x-ray magnetic circular dichroism can check the magnetic behavior of a buried FM layer.[13,14] However, all these methods require large-scale instruments, and their ability to perform selective magnetic measurements at several in-depth levels have not been yet demonstrated.

In this paper, we show how the Kerr effect can be used to separate the magnetization of several FM layers stacked in a multilayer structure. We consider only the Kerr effect linear in magnetization, neglecting second-order magneto-optical (MO) effects like the Voigt effect.[15,16] In Sec. I, we present a graphical representation of the Kerr effect in the rotation-ellipticity plane. In Sec. II we recall an analytical expression of the Kerr effect in the ultrathin FM layer approximation and discuss the possible ways for separating Kerr contributions coming from polar, longitudinal, or transverse magnetization components. From this separation, one can obtain the magnetization orientation separately in each FM layer. This is especially important in the case of dynamic measurements. Then we introduce the depth sensitivity function and present its main properties. In Sec. III, we show how to

 

assign each Kerr contribution to a given FM layer in a system where the Kerr hysteresis loop is a superposition of all Kerr contributions coming from different FM layers. Phase arguments in the $\theta\epsilon$ plane allow such an assignment. In Sec. IV, the separation of Kerr signals in a FM bilayer structure is treated within a general formalism. Section V solves this problem for FM trilayer structures when conveniently choosing the photon energy, the incidence angle, or the compensator phase shift. If the Kerr signal separation cannot be easily obtained, a general cascade numerical projection method is proposed in Sec. VI to decompose a global Kerr hysteresis loop into all individual FM contributions. Finally, a design of a multivalued MO recording structure is proposed, where the Kerr effect can read independently of the magnetization state of each of four storage layers located at different depths.

## I. COMPLEX REPRESENTATION OF THE KERR EFFECT

State of the art MO setups independently measure the Kerr rotation $\theta$ and Kerr ellipticity $\epsilon$.[16,17] Assuming weak MO effects, the complex Kerr effect $\Phi=\theta+i\epsilon=\Omega e^{i\xi}$ can be defined as a ratio between off-diagonal and diagonal reflectivity coefficients for the considered film structure. For an incident light polarized parallel ($p$ polarized) or perpendicular ($s$ polarized) to the plane of incidence, the complex $s$- and $p$-Kerr effects are defined as

$$\Phi_s=-\frac{r_{ps}}{r_{ss}}=\theta_s+i\epsilon_s=\Omega_s e^{i\xi_s}, \tag{1}$$

$$\Phi_p=\frac{r_{sp}}{r_{pp}}=\theta_p+i\epsilon_p=\Omega_p e^{i\xi_p}, \tag{2}$$

where $r_{x,y}$ are the reflectivity coefficients relative to the directions $x,y=\{s,p\}$. In another way, the Kerr effect $\Phi=\Omega e^{i\xi}$ is described by the Kerr amplitude $\Omega$ and Kerr phase $\xi$.

The experimental setup allowing one to measure the quantities defined in Eqs. (1) and (2), can be realized, for example, by modulating the light polarization state by the following optical arrangement: light source $\rightarrow$ polarizer $\rightarrow$ sample $\rightarrow$ photoelastic modulator (working at frequency $f$) $\rightarrow$ analyzer $\rightarrow$ detector.[17] Then the signals $s(2f)$ or $s(f)$, detected at the $2f$ or $f$ frequency are respectively related to Kerr rotation $\theta$ or ellipticity $\epsilon$.

The complex Kerr effect $\Phi$ can be visualized as a Kerr vector in the complex plane, here called the $\theta\epsilon$ plane. For small $\theta$, $\epsilon$, the $\theta\epsilon$ plane used for an analysis of the depth sensitivity corresponds to a small region of Cartesian complex plane of polarization around the point representing the polarization of the incident wave.[18] The representation of the Kerr effect on the $\theta\epsilon$ plane fulfills the following properties [Fig. 1(a) and 1(b)].

(i) The projection of the Kerr vector on the real axis gives the Kerr rotation $\theta$, and that the imaginary axis the Kerr ellipticity $\epsilon$. The length of the Kerr vector corresponds to the Kerr amplitude $\Omega$ and its orientation to the Kerr phase $\xi$. For the $p$-Kerr effect, the Kerr amplitude $\Omega_p=|E_s^{(r)}|/|E_p^{(r)}|$ is the ratio between the electric field for $s$ and $p$ reflected light, and the Kerr phase is equal to the phase shift between these waves, $\xi_p=\arg(E_s^{(r)})-\arg(E_p^{(r)})$.

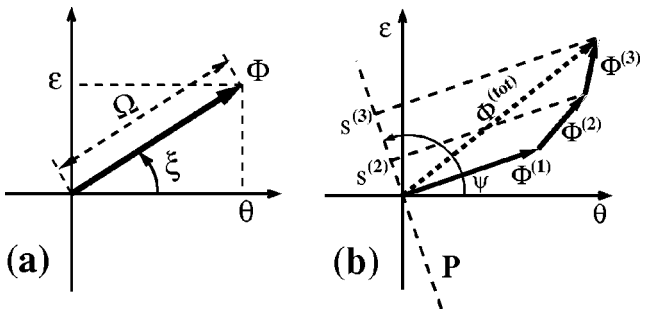


FIG. 1. Visualization of the Kerr effect in the $\theta\epsilon$ plane. (a) The Kerr vector $\Phi$ is described by the Kerr rotation $\theta$ and Kerr ellipticity $\epsilon$ or by the Kerr amplitude $\Omega$ and Kerr phase $\xi$. (b) The measured Kerr signal $s^{(i)}$ for each FM layer is obtained from the *projection* of the Kerr vector $\Phi^{(i)}$ on the projection axis $P$, the orientation of which is determined by a projection angle $\psi$.

(ii) For a given multilayer structure, the Kerr effect $\Phi^{(i)}$ originating from the $i$th layer is proportional to components of the related normalized magnetization $\boldsymbol{m}^{(i)}=[m_x^{(i)},m_y^{(i)},m_z^{(i)}]$. Since at first perturbation order in magnetization the Kerr effect is insensitive to the transverse component $m_x$ [see Eqs. (9) and (10) or Ref. 16], the total measured Kerr effect $\Phi^{(\mathrm{tot})}$ is given by a sum of all individual polar $\Phi_{\mathrm{pol}}^{(i)}$ and longitudinal $\Phi_{\mathrm{lon}}^{(i)}$ contributions,

$$\Phi^{(\mathrm{tot})}=\sum_i \Phi_{\mathrm{pol}}^{(i)}m_z^{(i)}+\sum_i \Phi_{\mathrm{lon}}^{(i)}m_y^{(i)}, \tag{3}$$

where the $z$ axis is defined to be normal to the film plane, and the $x$ and $y$ axes are both in the plane of the film, $x$ being perpendicular to the plane of the incidence of the light (the axis definition is shown in Fig. 2). The additivity of the Kerr effect is represented in Fig. 1(b) by the summation of Kerr vectors for all individual FM layers.

(iii) In the most general case, the experimental setup measures a Kerr signal $s$, which is the projection of the complex Kerr effect $\Phi$ onto a projection axis making an angle $\psi$ with the real axis $\theta$ [see Fig. 1(b)]:

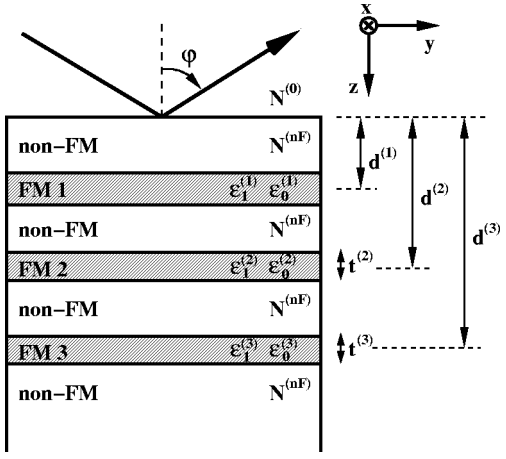


FIG. 2. Sketch of the considered FM multilayer structure.

TABLE I. Dependence of the projection angles $\psi$ on the compensator phase shift $\delta$.

| projection angle $\psi$ | expt. setup measures: Kerr rotation $\psi_0=0$ | Kerr ellipticity $\psi_0=\pi/2$ |
|---|---|---|
| Kerr *s* effect | $\delta$ | $\pi/2+\delta$ |
| Kerr *p* effect | $-\delta$ | $\pi/2-\delta$ |

$$s=\Re\mathrm{e}(\Phi e^{-i\psi}). \tag{4}$$

If the projection axis is parallel to the real axis ($\psi=0$), then the Kerr rotation $s=\theta=\Re\mathrm{e}(\Phi)$ is measured. If the projection angle is $\psi=\pi/2$, one measures the Kerr ellipticity $s=\epsilon=\Im\mathrm{m}(\Phi)=\Re\mathrm{e}(\Phi e^{-i\pi/2})$.

The variation of the projection angle $\psi$ can be realized with a Bobinet-Soleil compensator, giving a phase shift $\delta$, placed on the reflected light beam (i.e., in the case of the MO setup described above, the compensator is placed between the photoelastic modulator and the sample). The fast and slow axes of the compensator coincide with the *s* and *p* directions. Then the Kerr signal is modified according to the change of the effective reflection matrix $\boldsymbol{R}'$ having components $r'_{xy}$, where $\{x,y\}=\{s,p\}$ for the compensator-sample set:

$$\boldsymbol{R}'=\begin{pmatrix} e^{i\delta/2} & 0 \\ 0 & e^{-i\delta/2}\end{pmatrix}\begin{pmatrix} r_{ss} & r_{sp} \\ r_{ps} & r_{pp}\end{pmatrix}=\begin{pmatrix} r_{ss}e^{i\delta/2} & r_{sp}e^{i\delta/2} \\ r_{ps}e^{-i\delta/2} & r_{pp}e^{-i\delta/2}\end{pmatrix}. \tag{5}$$

Hence without a compensator one measures the Kerr signal $s_0=\Re\mathrm{e}(\Phi e^{-i\psi_0})$, and the Kerr detected signals $s_s$ and $s_p$ in the presence of the compensator are [Eqs. (1), (2), (4), and (5)]:

$$s_s=\Re\mathrm{e}\left(-\frac{r'_{ps}}{r'_{ss}}e^{-i\psi_0}\right)=\Re\mathrm{e}(\Phi_s e^{-i\delta}e^{-i\psi_0})=\Re\mathrm{e}(\Phi_s e^{-i\psi}), \tag{6}$$

$$s_p=\Re\mathrm{e}\left(\frac{r'_{sp}}{r'_{pp}}e^{-i\psi_0}\right)=\Re\mathrm{e}(\Phi_p e^{i\delta}e^{-i\psi_0})=\Re\mathrm{e}(\Phi_p e^{-i\psi}). \tag{7}$$

The projection angles $\psi$ are related to the compensator phase shift $\delta$ according to Table I.

## II. IN-DEPTH SENSITIVITY OF THE KERR EFFECT

Due to the attenuation of light inside the multilayer structure, FM layers placed at different depths contribute differently to the total Kerr effect. This argument was originally pointed out by Hubert and co-workers[5,19] to analyze the MO in-depth sensitivity in a thick FM film.

This section presents, first, analytical expressions of polar and longitudinal Kerr effects in multilayers consisting of ultrathin FM layers separated by nFM spacer layers. Then the in-depth sensitivity function $q$ is introduced, and its spectral and angular dependence analyzed. The depth sensitivity function is checked experimentally on the Au/Co system. Finally, the in-depth sensitivity for the case of the transverse Kerr effect is discussed.

### A. General analytical expression of the Kerr effect

In this section we express the Kerr effect of a multilayer structure composed of ultrathin FM layers with a thickness $t^{(i)}$ located at a depth $d^{(i)}$ and separated by nFM spacer layers consisting of the same nFM material as the substrate (Fig. 2). The thickness of the nFM layers can eventually be set to zero. The label $i$ increases with the in-depth position $d^{(i)}$ of the considered ultrathin FM layer.

If system contains one FM layer, ultrathin means that $t^{(1)}\ll\lambda/\mathrm{abs}[4\pi(\varepsilon_0^{(1)})^{1/2}]\approx 10$ nm,[20–22] because ultrathin means that profile of electrical field having incident polarization in the nFM material is not influenced by a presence of ultrathin FM layers. Thus, if a structure contains several FM layers, the condition of ultrathin approximation can be written as $\Sigma_i 4\pi t^{(i)}\mathrm{abs}[(\varepsilon_0^{(i)})^{1/2}]\ll\lambda$.

The superstrate (often air) has a refractive index $N^{(0)}$, and the light (photon energy $E$, vacuum wavelength $\lambda$) falls onto the sample under an incidence angle $\varphi$. The light wave vector is assumed to be located in the *z*-*y* plane of the considered Cartesian referential. The sign convention of time dependence is assumed to be $\exp[-i\omega t]$. The permittivity of all nFM layers and the substrate, $\varepsilon^{(nF)}=(N^{(nF)})^2$, is assumed to be isotropic. The permittivity tensor for the $i$th FM layer is expressed as[16,21]

$$\boldsymbol{\varepsilon}^{(i)}=\begin{pmatrix} \varepsilon_0^{(i)} & -i\varepsilon_1^{(i)}m_z^{(i)} & i\varepsilon_1^{(i)}m_y^{(i)} \\ i\varepsilon_1^{(i)}m_z^{(i)} & \varepsilon_0^{(i)} & -i\varepsilon_1^{(i)}m_x^{(i)} \\ -i\varepsilon_1^{(i)}m_y^{(i)} & i\varepsilon_1^{(i)}m_x^{(i)} & \varepsilon_0^{(i)}\end{pmatrix}. \tag{8}$$

Then, the *s*- and *p*-Kerr effects $\Phi_s^{(i)}$ and $\Phi_p^{(i)}$, originating from the $i$th FM layer, are[5,21]

$$\begin{aligned}\Phi_s^{(i)}&\equiv-\frac{r_{ps}}{r_{ss}}=\chi Q(d^{(i)})V_s t^{(i)} \\ &\quad\times\left[\varepsilon_1^{(i)}\frac{N_z^{(nF)}}{N^{(nF)}}m_z^{(i)}-\varepsilon_1^{(i)}\frac{N_y N^{(nF)}}{\varepsilon_0^{(i)}}m_y^{(i)}\right] \\ &=\Phi_{\mathrm{pol},s}^{(i)}m_z^{(i)}+\Phi_{\mathrm{lon},s}^{(i)}m_y^{(i)},\end{aligned} \tag{9}$$

$$\begin{aligned}\Phi_p^{(i)}&\equiv\frac{r_{sp}}{r_{pp}}=\chi Q(d^{(i)})V_p t^{(i)} \\ &\quad\times\left[\varepsilon_1^{(i)}\frac{N_z^{(nF)}}{N^{(nF)}}m_z^{(i)}+\varepsilon_1^{(i)}\frac{N_y N^{(nF)}}{\varepsilon_0^{(i)}}m_y^{(i)}\right] \\ &=\Phi_{\mathrm{pol},p}^{(i)}m_z^{(i)}+\Phi_{\mathrm{lon},p}^{(i)}m_y^{(i)},\end{aligned} \tag{10}$$

where $N_y=N^{(0)}\sin\varphi$ and $N_z^{(nF)}=\sqrt{\varepsilon_0^{(nF)}-N_y^2}$ correspond to the *y* and *z* components of the normalized wave vector in the nFM material. The optical coefficient $\chi$ in Eqs. (9) and (10),

$$\chi = \frac{2N^{(0)}(\omega/c)}{N^{(nF)2} - N^{(0)2}} = \frac{4\pi}{\lambda} \frac{N^{(0)}}{(N^{(nF)2} - N^{(0)2})}, \qquad (11)$$

describes the influence of the nFM substrate on the Kerr effect at normal incidence angle ($\varphi = 0$). More precisely, the term $\chi \varepsilon_1^{(i)} t^{(i)}$ is associated with the polar Kerr effect at $\varphi = 0$ for an ultrathin FM layer with thickness $t^{(i)}$ deposited on the top of the nFM bulk material. The term $(N_z^{(nF)}/N^{(nF)})V$ describes the variations of Kerr effect with incidence angle $\varphi$. For the *s*- or *p*-Kerr effect, $V$ has the forms

$$V_s = \frac{N^{(nF)} \cos\varphi}{N_z^{(nF)} \cos\varphi + N^{(0)} \sin^2\varphi}, \quad V_p = \frac{N^{(nF)} \cos\varphi}{N_z^{(nF)} \cos\varphi - N^{(0)} \sin^2\varphi}. \qquad (12)$$

At zero angle of incidence, $V_s = V_p = 1$. The term $Q(d^{(i)})$ describes the attenuation of the Kerr effect with the in-depth position of the FM layer $d^{(i)}$:

$$Q(d^{(i)}) = \exp[4i\pi N_z^{(nF)} (d^{(i)}/\lambda)]. \qquad (13)$$

The term $Q$ is independent on polarization of the incident light. Furthermore, as shown below, $Q$ depends weakly on the incidence angle $\varphi$.

### B. Separation of polar, longitudinal and transversal Kerr signals

The polar and longitudinal Kerr effects are related to the out-of-plane and in-plane magnetization components $m_z^{(i)}$ and $m_y^{(i)}$ of the FM layers, respectively. A separation of magnetization components is required if, for example, one wishes to measure the dynamical behavior of the magnetization reversal independently for several uncoupled or coupled FM layers in the structure.

The polar and longitudinal Kerr signals $s_{\text{pol}}^{(\text{tot})}$ and $s_{\text{lon}}^{(\text{tot})}$ can be separated by inversion of the incidence angle $\varphi$. Since the polar effect is even with $\varphi$, and the longitudinal effect odd with $\varphi$, $s_{\text{pol}}^{(\text{tot})}$ can be deduced from the sum of the Kerr signals $s^{(\text{tot})}(\varphi) + s^{(\text{tot})}(-\varphi)$ and $s_{\text{lon}}^{(\text{tot})}$ from their difference [Eqs. (9) and (10) or Ref. 23]. Another differentiation can be obtained from the Kerr signals $s_s^{(\text{tot})}$, $s_p^{(\text{tot})}$ measured as *s*- and *p*-Kerr effects for small incidence angles ($\varphi \approx 30°$). In this case, $V_s \approx V_p$ and thus [Eqs. (9) and (10)]

$$\Phi_{\text{pol},s}^{(i)} \approx \Phi_{\text{pol},p}^{(i)}, \quad \Phi_{\text{lon},s}^{(i)} \approx -\Phi_{\text{lon},p}^{(i)}. \qquad (14)$$

Hence $s_{\text{pol}}^{(\text{tot})}$ can be obtained from the sum $s_s^{(\text{tot})} + s_p^{(\text{tot})}$, and $s_{\text{lon}}^{(\text{tot})}$ from their difference.

The transverse $m_x$ component of the magnetization can be measured by the transverse Kerr effect (discussed later in Sec. II E), or by rotating the sample and magnet by 90° around the $z$ axis to measure $m_x$ in the longitudinal Kerr configuration. Once the polar, longitudinal, and transverse Kerr contributions are separated, the Kerr signals $s_{\text{pol}}^{(\text{tot})}$, $s_{\text{lon}}^{(\text{tot})}$, and $s_{\text{tra}}^{(\text{tot})}$ depend only on the in-depth profile of $m_z^{(i)}$, $m_y^{(i)}$, and $m_x^{(i)}$ magnetization components, respectively. Then, the magnetization component of each FM layer can be obtained through the procedures discussed in the following sections. Because the separation of polar, longitudinal, and transverse Kerr signals and the determination of their profiles are different problems, the polar and longitudinal depth sensitivity functions are studied separately below.

### C. Depth sensitivity function

The definition of the depth sensitivity function has been first introduced by Hubert *et al.*[19] We generalize it to multilayer structures and define the depth sensitivity function $q$ as the ratio of Kerr effects originating from the $i$th FM layer and first FM layer:

$$q^{\langle i,1\rangle} = \frac{\Phi^{(i)}}{\Phi^{(1)}} = \frac{\Omega^{(i)}}{\Omega^{(1)}} e^{i\Delta\xi^{\langle i,1\rangle}}. \qquad (15)$$

The depth sensitivity function $q$ can be visualized in the $\theta\epsilon$ plane as follows: $\arg(q^{\langle i,1\rangle}) = \xi^{(i)} - \xi^{(1)} = \Delta\xi^{\langle i,1\rangle}$ expresses the phase angle between the $i$th and first Kerr vectors. Furthermore, $|q^{\langle i,1\rangle}| = \Omega^{(i)}/\Omega^{(1)}$ gives the ratio of Kerr amplitudes for the $i$th and first first FM layers.

In the ultrathin film approximation, the polar $q_{\text{pol}}^{\langle i,1\rangle} = \Phi_{\text{pol}}^{(i)}/\Phi_{\text{pol}}^{(1)}$ and longitudinal $q_{\text{lon}}^{\langle i,1\rangle} = \Phi_{\text{lon}}^{(i)}/\Phi_{\text{lon}}^{(1)}$ depth sensitivity functions are analytically expressed from Eqs. (9) and (10) (Refs. 5 and 19):

$$q_{\text{pol}}^{\langle i,1\rangle} = \frac{t^{(i)}}{t^{(1)}} \frac{\varepsilon_1^{(i)}}{\varepsilon_1^{(1)}} Q(\Delta d^{\langle i,1\rangle}) \qquad (16)$$

and

$$q_{\text{lon}}^{\langle i,1\rangle} = \frac{t^{(i)}}{t^{(1)}} \frac{\varepsilon_1^{(i)} \varepsilon_0^{(1)}}{\varepsilon_1^{(1)} \varepsilon_0^{(i)}} Q(\Delta d^{\langle i,1\rangle}), \qquad (17)$$

where $\Delta d^{\langle i,1\rangle} = d^{(i)} - d^{(1)}$ is spacer thickness. The only difference between polar and longitudinal depth sensitivity functions comes from the extra term $\varepsilon_0^{(1)}/\varepsilon_0^{(i)}$.

Both depth sensitivity functions [Eqs. (16) and (17)] are products of three terms.

(i) The ratio of FM layers thicknesses $t^{(i)}/t^{(1)}$. This is a constant for a given film structure.

(ii) The quotient of the permittivities $\varepsilon_1^{(i)}/\varepsilon_1^{(1)}$ for $q_{\text{pol}}^{\langle i,1\rangle}$ and $(\varepsilon_0^{(1)}\varepsilon_1^{(i)})/(\varepsilon_0^{(i)}\varepsilon_1^{(1)})$ for $q_{\text{lon}}^{\langle i,1\rangle}$: this term differs from unity only if FM layers are made up of different materials. In that case, the value of this contribution can only be changed by varying the photon energy.

(iii) The contribution $Q(\Delta d^{\langle i,1\rangle})$ describes the influence of the nFM spacer layers. The Kerr phase angle between the $i$th and the first Kerr vectors introduced by nFM spacer layers is *increased* by [Eq. (13)]

$$(\Delta\xi^{\langle i,1\rangle})_{\text{spacer}} = \arg[Q(\Delta d^{\langle i,1\rangle})] = 4\pi \Re\text{e}(N_z^{(nF)}) \frac{\Delta d^{\langle i,1\rangle}}{\lambda}, \qquad (18)$$

where, as stated previously, $\Re\text{e}(N_z^{(nF)}) > 0$. Similarly, the absorbing spacer material attenuates the $i$th Kerr amplitude $\Omega^{(i)}$ by

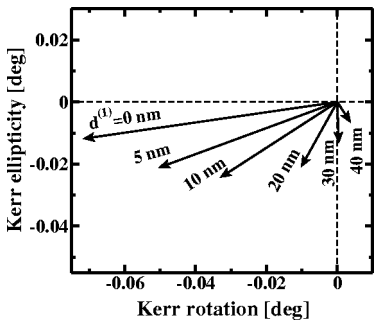


FIG. 3. Variation of the Kerr vector with increasing overlayer thickness $d^{(1)}$ for the Au($d^{(1)}$)/Co(1 nm)/Au system, calculated for $\varphi=0°$ and $E=3$ eV.

$$|q^{\langle i,1\rangle}|_{\text{spacer}}=|Q(\Delta d^{\langle i,1\rangle})|=\exp\left[-4\pi\Im\text{m}(N_z^{(nF)})\frac{\Delta d^{\langle i,1\rangle}}{\lambda}\right], \tag{19}$$

where $\Im\text{m}(N_z^{(nF)})>0$. If FM layers are made of the same material, the Kerr phase $\xi^{(i)}$ increases monotonically with *i*, i.e., with the in-depth location of the FM layer. At the same time, the normalized Kerr amplitude $\Omega^{(i)}/t^{(i)}$ decreases monotonically. The physical reason for this is that if the FM layer is located more deeply, the optical path is longer for reaching the FM layer (it increases $\xi$) and the light is more absorbed (it decreases $\Omega$). These statements will be used in Secs. III A and III B to associate a given Kerr contribution to a selected FM layer in the structure. As an example, the evolution of the Kerr vector in the $\theta\epsilon$ plane, with increasing thickness of the Au overlayer in the Au($d^{(1)}$)/Co(1 nm)/Au structure (the Co layer being perpendicularly magnetized) is calculated for $\varphi=0°$ and $E=3$ eV (Fig. 3). As the FM layer is located deeper in the multilayer stack, the Kerr vector rotates anti-clock-wise and its length decreases.

The agreement between the experimentally and theoretically determined polar depth sensitivity function $q_{\text{pol}}$ is presented in Sec. II D for the $(\text{Au/Co})_2$ system. If ultrathin FM layers consist of the same material, the depth sensitivity function *q* can be modified only by a change of term *Q*, which is *independent* of the material and thicknesses of FM layers. For a given multilayer structure (i.e., for a given spacer material and a given spacer thickness), the value of term *Q* can be modified only from a change of the photon energy *E* or the incidence angle $\varphi$. Consequently, the spectral and angular dependences of *Q* have to be studied in detail.

The spectral dependence of *Q*, for a 1-nm-thick spacer layer, is depicted in Figs. 4(a) and 4(b) for several common metals and $Si_3N_4$. As expected, (i) there is no damping [$\text{abs}(Q)=1$] for transparent materials, such as $Si_3N_4$. Noble metals cause a decrease of the Kerr amplitude by about 7% per nm of spacer thickness [$\text{abs}(Q)\approx 0.93$]. Because noble metals are more transparent in the vicinity of their plasma edge, the value of *Q* is larger here. This can be seen in Fig. 4(a) for Au at 2.5 eV and Ag at 3.8 eV. (ii) Figure 4(b) shows that the variation of the Kerr phase $\Delta\xi=\arg(Q)$ depends strongly on the photon energy and can vary up to 4° per nm of spacer thickness. The noble metals exhibit very small Kerr phase shift $\xi$ for photon energies below the plasma edge.

Because *Q* depends weakly on the incidence angle $\varphi$, it is convenient to define the renormalized quantity

$$p^{\langle i,1\rangle}(\varphi)=\frac{Q(\varphi,\Delta d^{\langle i,1\rangle})}{Q(\varphi=0,\Delta d^{\langle i,1\rangle})}\approx 1-2\pi i\frac{(N^{(0)})^2}{N^{(nF)}}\frac{\Delta d^{\langle i,1\rangle}}{\lambda}\sin^2\varphi, \tag{20}$$

where one uses the approximation $N_z^{(nF)}\approx N^{(nF)}-N^{(0)2}/(2N^{(nF)})\sin^2\varphi$. Equation (20) shows that the angular dependence of *Q* is given by $\sin^2\varphi$. The spectral variation of $p(\varphi=70°)$ for a 1-nm-thick spacer layer is depicted in Figs. 5(a) and 5(b) for several materials if the probing light comes from a vacuum ($N^{(0)}=1$). Then some remarks arise: (i) As can be seen from a comparison between Figs. 4 and 5, in general, the dependence of *Q* on the incidence angle is approximately ten times weaker than that found when changing the photon energy. The associated physical reason is that *Q* depends on the incidence angle $\varphi$ only through a variation of $N_z(\varphi)$, which is quite weak (about 10% between $\varphi=0$ and $\varphi=90°$). This reflects the fact that metals are optically denser materials than a vacuum, and consequently the light is always refracted in the multilayer close to the film normal. More quantitatively, an increase of the incidence angle from $\varphi=0$ to $\varphi=70°$ shortens the Kerr vector by about 0.5%, and increases its phase shift by about 0.3° per nm of spacer thickness [Figs. 5(a) and 5(b)]. (ii) Larger values of *p* are reached at higher photon energies. (iii) As can be seen from Eq. (20), *p* depends quadratically on $N^{(0)}$. Hence the dependence of *Q* on $\varphi$ can be enhanced if the incident light comes from an optically denser medium, for example, using a half-cylinder coupler contacted optically to the sample by an immersion liquid. For a coupling with $N^{(0)}=1.8$, the variation of *q* with the incidence angle increases about three times, and then the depth resolution achievable with variable angle of

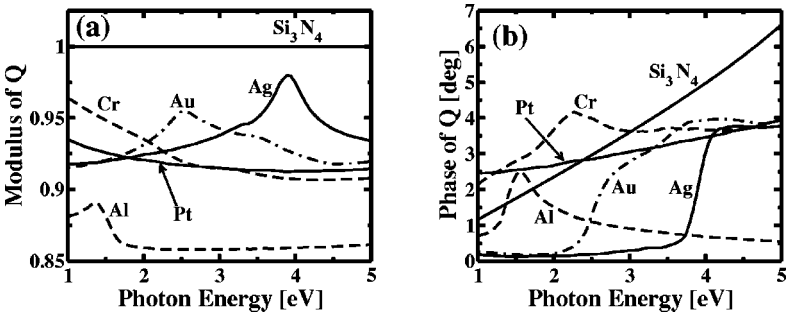


FIG. 4. Photon energy dependence of (a) the modulus and (b) the phase of *Q* [defined in Eq. (13)] in the case of a 1-nm-thick spacer layer of different materials.

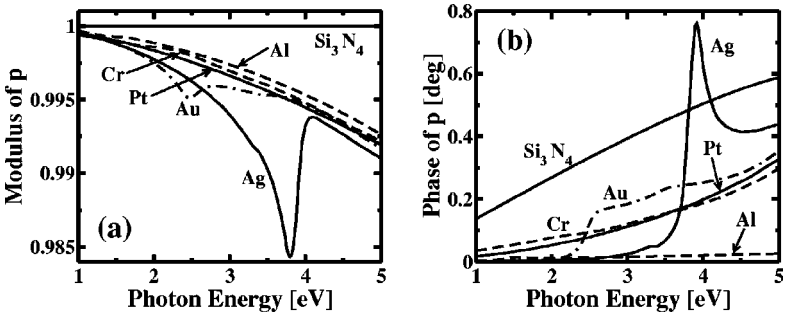


FIG. 5. Photon energy dependence of (a) the modulus and (b) the phase of $p=Q(70°)/Q(0°)$ defined in Eq. (20), in the case of a 1-nm-thick spacer layer of different materials.

incidence would be only about three times smaller than the resolution with photon energy.

The smaller sensitivity of $q$ to the angle of incidence $\varphi$ is balanced by the fact that it is linked to the optical and MO parameters at a single fixed photon energy. This may be convenient in some cases for two reasons. First, the variations of optical and MO parameters with photon energy are generally not known with enough accuracy. Second, this method does not require a spectroscopic equipment; thus one can use a laser as a light source. However, this magnetic in-depth detection requires $\varphi$ to vary over a large angle. Thus, in this paper, we prefer to focus our analysis on an in-depth resolution employing a variation of the photon energy. The advantages of this method are the previously mentioned higher depth resolution and the use of a fixed experimental geometry.

The depth sensitivity function $q$ is the only quantity sensitive to the difference between Kerr effects originating from different FM layers. The other parameters $\chi$ and $V_{s(p)}$, that describe the spectral and incidence angle variations of the Kerr effect [Eqs. (9) and (10)] are *the same* for *all* FM layers. For example, the change of the incidence angle $\varphi$ strongly modifies, but in a similar fashion, all Kerr vectors in the $\theta\epsilon$-plane. This is demonstrated on Fig. 6, which gives the calculated variation of Kerr vectors in the Au(5 nm)/Co(1 nm)/Au(5 nm)/Co(1 nm)/Au(bulk) system for different photon energies [Fig. 6(a)] and for different incidence angles [Fig. 6(b)]. Here we can immediately see that although spectral and angular variations of Kerr vectors are important, their *relative variation* is rather weak. This explains why the separation of Kerr signals originating from a given FM layer in a stack of several FM layers is not a trivial task, and why an inspection of the depth sensitivity function $q$ is so important.

### D. Experimental determination of $q_{\mathrm{pol}}$ for the $(\mathrm{Au/Co})_2$ system

This section deals with an experimental determination of the depth sensitivity function $q_{\mathrm{pol}}$ of the $(\mathrm{Au/Co})_2$ system, and its comparison with calculations based on analytical formula (16) and on the matrix formalism.[20,21] The studied structure is Au(5 nm)/Co(1.2 nm)/Au(3 nm)/Co(0.8 nm)/Au(25 nm) deposited on float glass [Fig. 7(a)]. The sample preparation and structural characteristics were reported in Ref. 24 and references therein. Both Co layers have a perpendicular magnetic anisotropy and exhibit square hysteresis loops; their thicknesses are different in order to obtain different coercive fields.[25] Consequently, it is easy to find magnitudes of the Kerr effect corresponding to 0.8- and 1.2-nm-thick Co layers. The Kerr effect coming from each Co layer is measured for incidence angles both at nearly normal incidence ($\varphi=7°$ for the Kerr $p$ effect) and at the incidence angle of 70° for both $s$- and $p$-Kerr effects. The polar Kerr loops are measured with applying the magnetic field along the easy anisotropy axis ($\boldsymbol{H}\|\hat{z}$). The spectral dependence of polar Kerr rotation and ellipticity at saturation are presented in Fig. 8 for each Co layer. Because of the small thickness of the Au spacer ($\Delta d^{\langle 2,1\rangle}=3$ nm), the two experimental Kerr spectra look similar within a scaling factor related to the

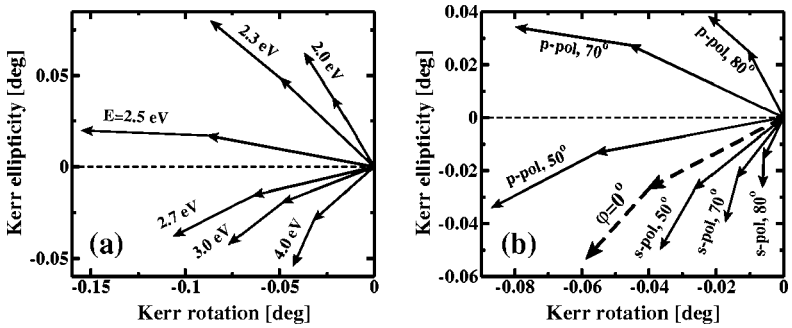


FIG. 6. Calculated variation of the Kerr effect in the $\theta\epsilon$ plane originating from both FM layers in the Au(5 nm)/Co(1 nm)/Au(5 nm)/Co(1 nm)/Au(bulk) system. (a) shows the variation of Kerr vectors at different photon energies for $\varphi=0$. (b) shows the variation of Kerr vectors for different incidence angles for both $s$ and $p$ polarizations at $E=3$ eV. Notice that an increase of the incidence angle gives an anticlockwise rotation of the $s$-Kerr effect, while it gives a clockwise rotation of the $p$-Kerr effect. Kerr vectors from both FM layers vary with $E$ and $\varphi$ in the $\theta\epsilon$ plane in a very similar way.

different Co layer thicknesses. From experimental values of the polar Kerr effects, $\Phi^{(1)}$ and $\Phi^{(2)}$, the quantity $q_{\mathrm{pol}}^{\langle 2,1\rangle}$ is deduced and presented in Fig. 9 in the complex form $|q|\exp[i\Delta\xi]$. We prefer to plot the normalized quantity $(t^{(1)}/t^{(2)})q_{\mathrm{pol}}^{\langle 2,1\rangle}$, that is comparable to calculations performed by analytical formulas (18) and (19) using $\Delta d^{\langle 2,1\rangle}=3$ nm. As well, it shows the $(t^{(1)}/t^{(2)})q_{\mathrm{pol}}^{\langle 2,1\rangle}=(\Phi^{(2)}t^{(1)})/(\Phi^{(1)}t^{(2)})$ variation, where Kerr effects $\Phi^{(1)}$ and $\Phi^{(2)}$ are calculated from the usual matrix formalism.[20]

We demonstrate that $(t^{(1)}/t^{(2)})q_{\mathrm{pol}}^{\langle 2,1\rangle}$ depends weekly on the incidence angle, $\varphi$ and is independent of the polarization of the incident light (Fig. 9); this result agrees with our previous expectations. The agreement between $(t^{(2)}/t^{(1)})q_{\mathrm{pol}}^{\langle 2,1\rangle}$, calculated from the matrix formalism and experimental data, is nearly perfect. Analytical formulas (18) and (19) well describe the variation of $q$. The weak difference between experimental data and analytical calculations comes from additional damping and phase shifts originating from Co layers, that are neglected in our simple treatment. This explains why the ultrathin film approximation predicts smaller damping (i.e., larger value of $|q|$) and smaller phase shift.

In conclusion, we can say that our analytical expressions of the depth sensitivity function $q_{\mathrm{pol}}^{\langle 2,1\rangle}$ [Eq. (16)] describes reasonably well the difference between Kerr effects originating from layers located at different depths, in the case of ultrathin FM metallic layers.

### E. Transverse Kerr effect

Let us now discuss briefly the transverse Kerr effect, which is only sensitive to the transverse component $m_x$ of the magnetization.[16] The transverse Kerr effect is a different physical quantity than the polar and longitudinal effects, because it is measured by a variation of the reflected light intensity for *p*-polarized incident light at oblique incidence (i.e., $\varphi\neq 0$).

In the linear expansion of reflection coefficients $r_{pp}$ with respect to transverse magnetization components $m_x^{(i)}$ in all FM layers, the total $r_{pp}^{(\mathrm{tot})}$ is

$$r_{pp}^{(\mathrm{tot})}=r_{pp,0}+\sum_i r_{pp,\mathrm{mag}}^{(i)}m_x^{(i)}, \tag{21}$$

where $r_{pp,0}$ is independent of the sample magnetization and $r_{pp,\mathrm{mag}}^{(i)}$ represents the contribution of the magnetized $i$th FM layer. The $r_{pp,\mathrm{mag}}^{(i)}$ coefficient can be written as

$$r_{pp,\mathrm{mag}}^{(i)}=q_{\mathrm{tra}}^{\langle i,1\rangle}r_{pp,\mathrm{mag}}^{(1)}, \tag{22}$$

where $q_{\mathrm{tra}}^{\langle i,1\rangle}$ is the transversal depth sensitivity function. In the ultrathin FM layer approximation, it can be found that $q_{\mathrm{tra}}^{\langle i,1\rangle}$ has exactly the same form as the longitudinal one $q_{\mathrm{tra}}^{\langle i,j\rangle}=q_{\mathrm{lon}}^{\langle i,j\rangle}$, defined by Eq. (17).

Because the $r_{pp,\mathrm{mag}}^{(i)}$ magnetic contribution is much smaller than $r_{pp,0}$, the reflected *p*-polarized light intensity $I_p\sim|r_{pp}|^2$ can be written as

$$I_p=I_{p,0}+\sum_i I_{p,\mathrm{mag}}^{(i)}\sim|r_{pp,0}|^2+s_{\mathrm{tra}}^{(\mathrm{tot})}. \tag{23}$$

Here $s_{\mathrm{tra}}^{(\mathrm{tot})}$ represents the total transverse Kerr signal, which is expressed as

$$s_{\mathrm{tra}}^{(\mathrm{tot})}=\sum_i s_{\mathrm{tra}}^{(i)}=2\sum_i \Re\mathrm{e}(q^{\langle i,1\rangle}r_{pp,\mathrm{mag}}^{(1)}r_{pp}^{\dagger})m_x^{(i)}$$

$$=2\sum_i \Re\mathrm{e}(q^{\langle i,1\rangle}\tilde{\Phi}^{(1)})m_x^{(i)}, \tag{24}$$

where $\tilde{\Phi}^{(1)}\equiv r_{pp,\mathrm{mag}}^{(1)}r_{pp,0}^{\dagger}$. The dagger sign denotes the complex conjugate. Equation (23) can be compared with Kerr signals $s^{(i)}=\Sigma_i\Re\mathrm{e}(q^{\langle i,1\rangle}\Phi^{(1)}m^{(i)}e^{i\psi})$ determined for polar and longitudinal Kerr effects [Eqs. (3), (4), and (15)]. Thus the transversal Kerr signal $s_{\mathrm{tra}}^{(i)}$ corresponds to the previous Kerr signal $s^{(i)}$. The only difference is that, in the case of the transverse Kerr effect, it is not possible to tune the projection angle by means of a compensator, and consequently the projection angle is fixed to $\psi=0$. It can be concluded that the transverse Kerr effect can also be used for in-depth sensitivity measurements, but at a fixed projection angle $\psi$.

## III. ASSIGNMENT OF KERR EFFECT CONTRIBUTION TO A FM LAYER LOCATED AT A GIVEN DEPTH

### A. Generalities

Let us consider the case of a multilayer structure composed of several ultrathin FM layers of the same FM material, providing nearly square magnetic hysteresis loops and separated by nFM spacer layers (Fig. 2). An open question is often to assign each loop to a particular FM layer located at a depth $d^{(i)}$. To solve this problem, let us recall results discussed from our examination of Eqs. (18) and (19): (i) The Kerr phase $\xi^{(i)}$ increases *monotonically* with an increasing in-depth position $d^{(i)}$ of the FM layer. (ii) For absorbing spacer materials $[\Im\mathrm{m}(N_z^{(nF)})>0]$, the normalized Kerr amplitude $\Omega^{(i)}/t^{(i)}$ decreases monotonically with increasing $d^{(i)}$.

Consequently, the procedure for determining the in-depth position of a FM layer is the following: (i) Hysteresis loops of both Kerr rotation $\theta$ and Kerr ellipticity $\epsilon$ are measured at the same photon energy $E$ and incidence angle $\varphi$. (ii) The value of the Kerr effect at saturation $\Phi^{(i)}=\theta^{(i)}+i\epsilon^{(i)}=\Omega^{(i)}e^{i\xi^{(i)}}$ is determined, experimentally for each FM layer; this is an easy procedure if the coercivity differs for each FM layer. (iii) The Kerr phase $\xi^{(i)}=\arg(\Phi^{(i)})$ is determined and (iv) the $\xi^{(i)}$ values are classified in a decreasing order; then the largest value of $\xi^{(i)}$ corresponds to the deepest FM layer. (v) The in-depth location of the FM layers can be confirmed from calculations of the normalized Kerr amplitudes $\Omega^{(i)}/t^{(i)}$, which must decrease with $d^{(i)}$. This analysis is valid for a large number of FM layers. The main limitation is when some FM layers exhibit the same coercive field. In such a case, a calculation using a general matrix formalism involving all information about optical and magneto-optical parameters has to be used.

If the FM layers do not consist of the same FM material, then the Kerr effects $\Phi^{(i)}$ have to be renormalized by $\varepsilon_1^{(i)}$ for the polar Kerr effect and by $\varepsilon_1^{(i)}/\varepsilon_0^{(i)}$ for the longitudinal Kerr

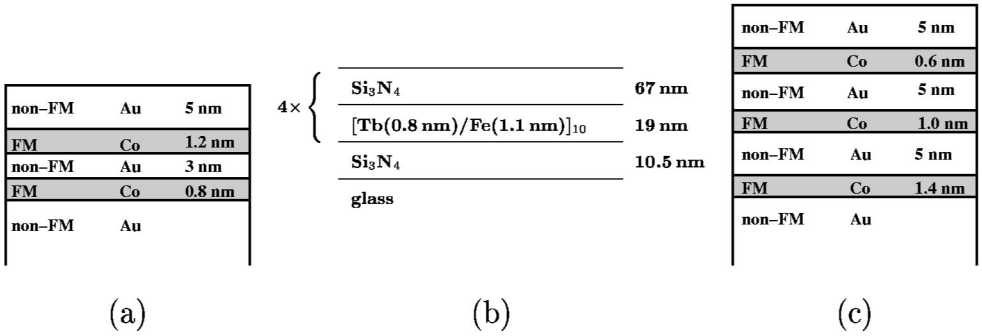


FIG. 7. Sketches of studied sample structures (a) $(Au/Co)_2$ (b) $(TbFe/Si_3N_4)_4$, and (c) $(Au/Co)_3$.

effect. Then the influence of different FM materials is avoided, as can be found from Eqs. (9) and (10).

In the case of thick spacer layers, the same rules are valid as well. The only problem is that the deduced value of the Kerr phase $\xi^{(i)}$ can be mistaken by a factor of $2\pi$, which can generate difficulties to classify the Kerr phases $\xi^{(i)}$. This is overcome when considering the normalized Kerr amplitude $\Omega^{(i)}/t^{(i)}$ or determining of the angular or spectral dependence of $\xi^{(i)}$. Since

$$\xi^{(i)} = \xi^{(1)} + \Delta\xi^{\langle i,1\rangle}, \tag{25}$$

where $\Delta\xi^{\langle i,1\rangle}$, in the ultrathin approximation of the FM layer, is

$$\Delta\xi^{\langle i,1\rangle} = \frac{4\pi}{\lambda}\Delta d^{\langle i,1\rangle}\Re\mathrm{e}(N_z^{(nF)}) > 0, \tag{26}$$

the deepest FM layer has the largest $\Delta d^{\langle i,1\rangle}$ and consequently the largest slope in the plots of $\xi^{(i)}$ with photon energy or incidence angle. This will be illustrated for the spectral dependence of Kerr phase $\xi^{(i)}$ of the $TbFe/Si_3N_4$ system, where the deepest reachable (the third) FM stack has the largest slope in the $\xi^{(i)}(E)$ dependence. The determination of the in-depth position of FM layers is reported in Sec. III B for the $(Au/Co)_3$ film structure.

### B. Application to the $(Au/Co)_3$ film structure

The Au(5 nm)/Co(0.6 nm)/Au(5 nm)/Co(1 nm)/Au(5 nm)/Co(1.4 nm)/Au(24 nm)/glass film structure is considered in this subsection. The sample is presented in Fig. 7(c) and its preparation and characterization were reported previously.[24] Because in our particular case the Co layers have increasing thicknesses and consequently decreasing coercivity,[25] it is initially easy to assign the Kerr loop contributions to the three Co layers.

From another side, it is possible to assign the different Kerr contributions from the saturated Kerr effect independently for each FM layer. Here they are determined at $E = 3.8$ eV from hysteresis loops measured by both Kerr rotation and ellipticity at nearly normal incidence ($\varphi = 7°$, the *p*-Kerr effect) in a magnetic field applied along the normal of the film ($\boldsymbol{H} \| \hat{z}$). These two loops are presented in the Fig. 10. The values of individual coercive fields and Kerr rotations and ellipticities corresponding to each FM layer are given in Table II.

The value of $\xi^{(i)}$ increases with *i*, while $\Omega^{(i)}/t^{(i)}$ decreases, proving that the depth location of the considered FM layer increases with *i*. Because both Au spacer layers have the same thickness $\Delta d^{\langle 2,1\rangle} = \Delta d^{\langle 3,2\rangle} = 5$ nm, the difference of Kerr phases are obviously equal $\Delta\xi^{\langle 2,1\rangle} = \Delta\xi^{\langle 3,2\rangle} = 30°$. The ratio between normalized Kerr amplitudes, $(\Omega^{(2)}/t^{(2)})/(\Omega^{(1)}/t^{(1)}) = 0.69$, $(\Omega^{(3)}/t^{(3)})/(\Omega^{(2)}/t^{(2)}) = 0.49$ should be the same, but they differ from each other, because the interface contributions to Kerr effect[24] were neglected here. Normalized Kerr amplitudes calculated from matrix formalism are $(\Omega^{(2)}/t^{(2)})/(\Omega^{(1)}/t^{(1)}) = 0.62$, $(\Omega^{(3)}/t^{(3)})/(\Omega^{(2)}/t^{(2)}) = 0.60$, thus the influence of different Co thicknesses is small.

## IV. SEPARATION OF KERR SIGNALS IN A FM BILAYER STRUCTURE

This section proposes ways to separate Kerr signals $s^{(1)}$ and $s^{(2)}$ of each FM layer in a structure consisting of two FM layers separated by a nFM spacer layer. In other words, we solve the problem of finding special MO arrangements to cancel either the Kerr signal contribution coming from one or the other FM layer. Using the representation of Kerr effect in the complex $\theta\epsilon$ plane, the contribution of the first or second FM layers ($s^{(1)}$ or $s^{(2)} = 0$) cancels if the Kerr vector $\Phi^{(1)}$ or $\Phi^{(2)}$ is *perpendicular* to the projection axis. This situation is depicted in Fig. 11(a) for canceling the Kerr contribution of the first FM layer. The angle between the Kerr vector $\Phi^{(i)}$ and the projection axis equals $\arg(\Phi^{(i)}) - \psi$. It can be tuned in several ways.

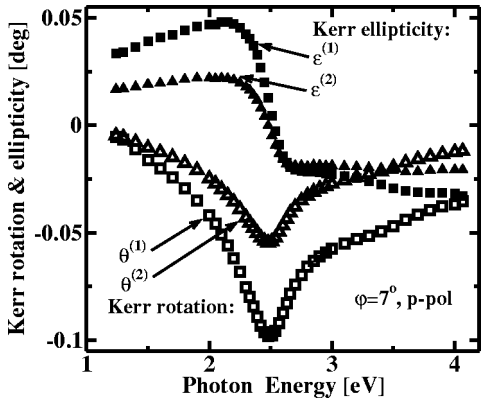


FIG. 8. Experimental polar Kerr rotation and ellipticity spectra for the $(Au/Co)_2$ system for each Co layer. The *p*-polarized measurements were performed at a nearly normal incidence ($\varphi = 7°$).

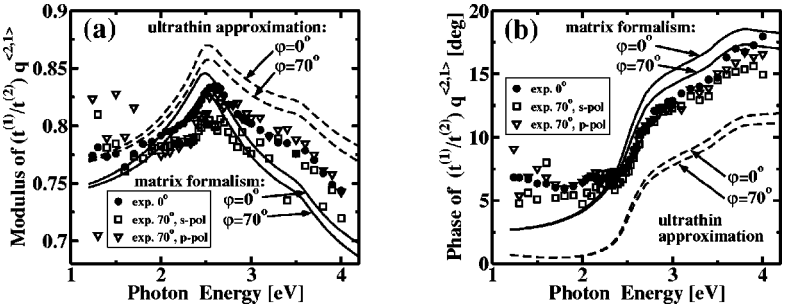


FIG. 9. Experimental values of the normalized depth sensitivity $(t^{(1)}/t^{(2)})q^{\langle 2,1\rangle} = (t^{(1)}/t^{(2)})(\Phi^{(2)}/\Phi^{(1)})$ as a function of the photon energy for $(Au/Co)_2$ at $\varphi=0$ and $\varphi=70°$ incidence. In the ultrathin Co layer approximation, it should correspond to $Q$ defined by Eq. (13) whose variation is represented by a dashed line. The full line shows the normalized depth sensitivity calculated from $\Phi^{(1)}$, $\Phi^{(2)}$ determined from the matrix formalism (Ref. 21).

(i) For a fixed projection angle $\psi$, the orientation of the Kerr vectors can be modified by varying the photon energy $E$ [Fig. 6(a)] (Ref. 7) or the angle of incidence $\varphi$ [Fig. 6(b)].[8] An example of the Kerr vector variations with $E$ or $\varphi$ in the complex $\theta\epsilon$ plane is reported in Fig. 6 for a Au/Co/Au/Co/Au structure. It shows how it is possible to find value of $E$ or $\varphi$ that gives either $\theta^{(i)}=0$ or $\epsilon^{(i)}=0$ individually for each of the two FM layers.

(ii) For fixed Kerr vectors in the complex $\theta\epsilon$ plane (i.e., for given values of $E$ and $\varphi$), the projection angle $\psi$ has to be tuned, for example with a Babinet-Soleil compensator (Sec. I of Ref. 9). Note that this elegant technique has been used in its microscopy mode to prove unambiguously the existence of a biquadratic coupling between Fe layers separated by a Cr spacer layer.[4]

(iii) In principle, it is not necessary to tune the projection angle $\psi$ experimentally, because the tuning can be done afterward numerically. From a knowledge of two Kerr signals $s_a$ and $s_b$, measured under different conditions (for example Kerr rotation and ellipticity or two Kerr signals measured at two different photon energies or incidence angles), it is possible to deduce the Kerr signal which originates only from the $i$th FM layer,

$$s^{(i)} = s_a \cos\psi^{(i)} + s_b \sin\psi^{(i)}, \tag{27}$$

where the weight of the linear combination of $s_a$ and $s_b$ is parametrized by the projection angle $\psi^{(i)}$. A similar approach was suggested in Ref. 26.

## V. SEPARATION OF KERR SIGNALS IN A FM TRILAYER STRUCTURE

### A. "Parallel Kerr vector" method

As discussed in Sec. IV, the Kerr effect of the $i$th layer can always be canceled if the corresponding Kerr vector $\Phi^{(i)}$ becomes perpendicular to the projection axis. Thus, for a FM trilayer structure, if one succeeds in setting up two Kerr vectors $\Phi^{(i)}$ and $\Phi^{(j)}$ parallel to each other and perpendicular to the projection axis, the measured Kerr signal depends only on the magnetization state of the last FM layer. The situation is presented in Fig. 11(b), where Kerr signals from the first and third FM layers are canceled simultaneously and, consequently, only the Kerr signal coming from the second FM layer is detected. We call this the "parallel Kerr vector" method. More generally, the $i$th and $j$th Kerr vectors are parallel if

$$\Delta\xi^{\langle i,j\rangle} = \xi^{(i)} - \xi^{(j)} = \arg(q^{\langle i,j\rangle}) = n\pi, \tag{28}$$

where $n$ is an integer. Considering a polar magnetized ultrathin FM film, the angle between two Kerr vectors is analytically expressed by [Eq. (16)]

$$\Delta\xi^{\langle i,j\rangle} = \frac{4\pi}{\lambda_0}\Delta d^{\langle i,j\rangle}\Re\mathrm{e}(N_z^{(nF)}) + \arg\left(\frac{\varepsilon_1^{(i)}}{\varepsilon_1^{(j)}}\right). \tag{29}$$

Just note that in the case of longitudinal magnetization, the second term in Eq. (29) becomes $\arg[(\varepsilon_1^{(i)}\varepsilon_0^{(j)})/(\varepsilon_1^{(j)}\varepsilon_0^{(i)})]$. Consequently, both terms appearing in Eq. (29) can be tuned to setup two parallel Kerr vectors simultaneously (i.e., $\Delta\xi^{\langle i,j\rangle}=n\pi$). If the two FM layers consist of different materials and if the distance $\Delta d^{\langle i,j\rangle}$ between these FM layers is small, then the main contribution to $\Delta\xi^{\langle i,j\rangle}$ comes from the second term, $\arg(\varepsilon_1^{(i)}/\varepsilon_1^{(j)})$, whose value can only be tuned by a photon energy variation.

If both the $i$th and $j$th FM layers are made of the same material, the only nonzero contribution to $\Delta\xi^{\langle i,j\rangle}$ comes from the first term of Eq. (29), requiring a certain distance $\Delta d^{\langle i,j\rangle}$ between the FM layers to realize $\Delta\xi^{\langle i,j\rangle}=n\pi$. For typical values of the photon energy and refractive indices of the nFM spacer layer ($E=3$ eV, $N^{(nF)}=2.5$), the minimum distance between FM layers required to obtain parallel Kerr vector configurations is as large as $\Delta d^{\langle i,j\rangle}\approx 40$ nm. As discussed in Sec. II C, the part of $\Delta\xi^{\langle i,j\rangle}$ originating from nonzero spacer thickness can be varied by changing either the photon energy or incidence angle (Figs. 3–6). However, in general, the variation of $\Delta\xi^{\langle i,j\rangle}$ with the incidence angle is weaker than that obtained by the photon energy variation, as discussed in Sec. II C.

The "parallel Kerr vector" method is particularly suitable for checking the individual single layer magnetizations in a multilayer structure where FM layers are made up by the same material and separated by thick nFM spacer layers, as demonstrated below for a typical magneto-optical recording multilayer $(TbFe/Si_3N_4)_4$.[26]

### B. Application to the $(TbFe/Si_3N_4)_4$ structure

As discussed in Sec. IV, the Kerr signals coming from two FM layers can be canceled simultaneously if the corresponding Kerr vectors are set parallel in the $\theta\epsilon$ plane. Such a configuration can be obtained by adjusting the photon energy. This section demonstrates how to separate individual Kerr signals originating from each FM layer in a FM trilayer structure.

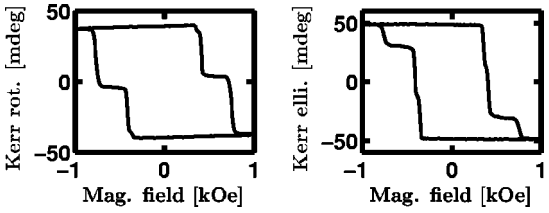


FIG. 10. Kerr rotation and Kerr ellipticity hysteresis loops measured on a $(Au/Co)_3$ system at $E=3.8$ eV and at a nearly normal incidence angle ($\varphi=7°$, *p*-Kerr effect). The external magnetic field was applied along the sample normal ($\boldsymbol{H}\|\hat{z}$).

The sample under investigation is $(Si_3N_4/TbFe)_4/Si_3N_4(10.5\ nm)$/glass, where TbFe represents a simple $[Tb(0.8\ nm)/Fe(1.1\ nm)]_{10}$ multilayer stack. TbFe stacks are separated by 67 nm of $Si_3N_4$ [Fig. 7(b)]. Information on the sample preparation is detailed elsewhere.[27,28] Each TbFe stack displays a perpendicular magnetic anisotropy. As is commonly observed,[29] in spite of having the same thickness the TbFe stacks usually exhibit slightly different coercive fields. All polar Kerr measurements have been performed at nearly normal incidence ($\varphi=7°$, the measured *p*-Kerr effect) in a magnetic field applied along the normal of the film ($\boldsymbol{H}\|\hat{z}$).

Although the sample consists of *four* stacks of TbFe, the third and fourth stacks have the same coercive field. This was verified by comparing the individual Kerr hysteresis loop amplitudes measured from the glass side[27] and the results of calculations performed in the frame of the matrix formalism.[21] Furthermore, carrying out polar Kerr measurements from the upper $Si_3N_4$ side, the fourth (deepest) TbFe stack is screened and exhibits a negligible MO contribution over the main spectral range. Thus in spite of the presence of four TbFe stacks, Kerr effect practically probes here only the three first FM stacks in the multilayer, allowing us to demonstrate how to separate Kerr signals coming from an equivalent *three* FM layer structure.

The first problem is to find photon energies, for which two individual Kerr vectors become parallel. Thus, the Kerr spectrum originating from each TbFe stack has been determined experimentally, but it can be deduced theoretically as well. Let us consider the hysteresis loops of the sample measured both in Kerr rotation and Kerr ellipticity in the 1.2–4.2-eV spectral range. Some of the Kerr rotation hysteresis loops are presented in Fig. 12. Since individual square loops exhibit different coercivities, it is straightforward to determine the maximum Kerr rotation and Kerr ellipticity for each of the three TbFe stacks of interest. On the entire photon energy range, the corresponding Kerr amplitudes $\Omega^{(i)}$ and Kerr phases $\xi^{(i)}$ are then deduced and represented in Figs. 13(a) and 13(b). As expected, the deepest FM stack shows the smallest normalized Kerr amplitude $\Omega^{(i)}/t^{(i)}$, and exhibits the largest slope in the spectral $\xi^{(i)}(E)$ variation. The spectra of Kerr amplitudes $\Omega^{(i)}(E)$ [Fig. 13(a)] show two interesting features: first, they show a pronounced maximum at 2.0 eV and secondly, the TbFe stacks become more transparent near 3.5 eV, and thus their Kerr amplitudes $\Omega^{(i)}$ become weak and comparable [see the inset of Fig. 13(a)].

The Kerr spectra can be as well represented in the complex $\theta\epsilon$ plane. This representation is shown in Fig. 14(a) over the 3.1–3.9-eV limited spectral range. For photon energy data represented by dashed lines, two Kerr vectors become nearly parallel to each other. To determine more precisely the photon energies at which two Kerr vectors become parallel, we have plotted the spectral dependence of the difference between Kerr phases $\Delta\xi^{\langle i,j\rangle}$ as a function of the photon energy [see Fig. 14(b)]. The Kerr vectors from the $i$th and $j$th TbFe stacks are obviously parallel if $\Delta\xi^{\langle i,j\rangle}=n\pi$. This condition is fulfilled for photon energies $E=3.32$ eV ($\Delta\xi^{\langle 3,1\rangle}=540°$), $E=3.53$ eV ($\Delta\xi^{\langle 2,1\rangle}=360°$) and $E=3.62$ eV ($\Delta\xi^{\langle 3,2\rangle}=360°$). Because in our sample the spacer layer thicknesses $d^{\langle 2,1\rangle}=d^{\langle 3,2\rangle}=67$ nm are equal, $\Delta\xi^{\langle 3,2\rangle}$ is obviously found experimentally close to $\Delta\xi^{\langle 2,1\rangle}$ [Fig. 14(b)]. This is not exactly true in the vicinity of 3.5 eV, where the TbFe stacks are more transparent, and thus the fourth TbFe stack slightly influences the $\Delta\xi^{\langle 3,2\rangle}$ value.

Thus we have chosen the photon energies to provide the parallelism between two Kerr vectors. We tuned the projection angle $\psi$ by a Bobinet-Soleil compensator (as discussed in Sec. I) to set the projection axis perpendicular to the two parallel Kerr vectors.

As example, at a given photon energy 3.53 eV, large modifications in the hysteresis loop shape are observed when changing the projection angle $\psi$ (Fig. 15). Most of the sample hysteresis loops are combinations of three individual Kerr loops. However, the hysteresis loop measured for $\psi=-21°$ corresponds only to the third TbFe stack, and Kerr signals coming from the first and second TbFe stacks are both canceled. Hence, choosing the photon energy $E$ and projection angle $\psi$ well, we succeeded in separating the hysteresis loop of each FM stack.

From loops presented in Fig. 15, we are able to determine the variation of Kerr signals $s^{(i)}$ coming from each TbFe stack as a function of the projection angle $\psi$ (Fig. 16). As expected from Eq. (4), $s^{(i)}=\Re e[\Phi^{(i)}\exp(i\psi)]$, the dependence of $s^{(i)}(\psi)$ is sinusoidal.[9] Sinusoidal full lines perfectly fit the experimental data (Fig. 16). Furthermore, one can verify that both Kerr signals $s^{(1)}$ and $s^{(2)}$ cancel simultaneously for $\psi=-21°$. This explains why only the Kerr signal originating from the third TbFe stack is measured at this

TABLE II. Kerr effect and coercive field of each FM layer in the $(Au/Co)_3$ system.

| | $H_c$ (Oe) | $\theta^{(i)}$ (m deg) | $\epsilon^{(i)}$ (m deg) | $\Omega^{(i)}$ (m deg) | $\xi^{(i)}$ (deg) | $t^{(i)}$ (nm) | $\Omega^{(i)}/t^{(i)}$ (m deg/nm) |
|---|---|---|---|---|---|---|---|
| $\Phi^{(1)}$ | 770 | −21.0 | −9.0 | 22.9 | 203° | 0.6 | 38.2 |
| $\Phi^{(2)}$ | 420 | −15.8 | −21.4 | 26.6 | 233° | 1.0 | 26.6 |
| $\Phi^{(3)}$ | 360 | −2.1 | −18.0 | 18.1 | 263° | 1.4 | 12.9 |

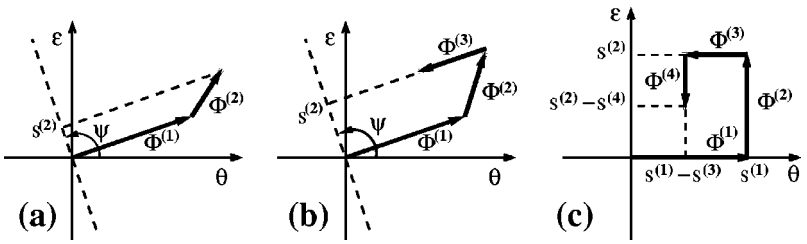


FIG. 11. Sketch of Kerr vectors and projection axis in the $\theta\epsilon$ plane when the Kerr signal comes from only one FM layer in a system consisting of (a) two and (b) three FM layers. (c) Kerr vector configuration used for volume MO readout with four FM recording layers (see Sec. VI E for details).

particular photon energy and projection angle. The resulting Kerr hysteresis loops, depending only on the magnetization state of the first, second and third TbFe stacks, were deduced (Fig. 17) by choosing an appropriate couple of $E$ and $\psi$ values.

## VI. LARGE NUMBER OF MAGNETIC LAYERS: "CASCADE NUMERICAL PROJECTION" METHOD

### A. General formalism

Considering the case of more than three FM layers and thin nFM spacer layers, it is generally not possible to separate the MO contributions by the ''parallel Kerr vector'' method. This is only possible for specially engineered structures as described later in Sec. VI E. This subsection treats the present problem from another point of view: the total Kerr effect is measured in different experimental conditions to obtain a set of independent measurements from which we calculate the Kerr signal coming from each FM layer. This numerical approach can be extended to a large number of FM layers.

A separation of polar, longitudinal, and transverse Kerr signals, $s_{\mathrm{pol}}^{(\mathrm{tot})}$, $s_{\mathrm{lon}}^{(\mathrm{tot})}$, and $s_{\mathrm{tra}}^{(\mathrm{tot})}$ has was already discussed in Sec. II B. Once separated, the Kerr signal depends on the profile of only one magnetization component $m_w^{(i)}$, $w=x$ or $y$ or $z$.

Let us consider a system with $N$ FM layers having polar magnetizations $m_z^{(i)}$, $i=1 \ldots N$. One assumes that $M$ polar Kerr signals $s_x^{(\mathrm{tot})}$, $x=1 \ldots M$, $M \geqslant N$ can be measured in independent experimental conditions. Independent means that experiments have to be carried out at different photon energies $E_x$, different incidence angles $\varphi_x$, or different projection angles $\psi_x$. The measured Kerr signals $s_x^{(\mathrm{tot})}$ are given by a sum of Kerr signal contributions $s_x^{(i)}$ from the $i$th FM layer weighted by the corresponding polar FM layer magnetization $m_z^{(i)}$. This relationship between $s_x^{(\mathrm{tot})}$ and $m_z^{(i)}$ can be written through an $X$-matrix[30]

$$\begin{pmatrix} s_1^{(\mathrm{tot})} \\ s_2^{(\mathrm{tot})} \\ \vdots \\ s_M^{(\mathrm{tot})} \end{pmatrix} = \begin{pmatrix} s_1^{(1)} & s_1^{(2)} & \cdots & s_1^{(N)} \\ s_2^{(1)} & s_2^{(2)} & \cdots & s_2^{(N)} \\ \vdots & \vdots & \ddots & \vdots \\ s_M^{(1)} & s_M^{(2)} & \cdots & s_M^{(N)} \end{pmatrix} \cdot \begin{pmatrix} m_z^{(1)} \\ m_z^{(2)} \\ \vdots \\ m_z^{(N)} \end{pmatrix}, \quad (30)$$

$$\boldsymbol{s}^{(\mathrm{tot})} = X \cdot \boldsymbol{\mu}.$$

Consequently, the FM layer magnetizations $m_z^{(i)}$ can be straightforwardly deduced by an inversion (for $M=N$) or pseudoinversion (for $M>N$) of the $X$ matrix:

$$\boldsymbol{\mu} = \widetilde{\mathrm{inv}}(X) \cdot \boldsymbol{s}^{(\mathrm{tot})}. \quad (31)$$

The pseudoinversion of $X$ means that Eq. (30) is solved in the sense of minimizing the least-square error, which is $||\boldsymbol{s}^{(\mathrm{tot})} - X \cdot \boldsymbol{\mu}||$.[31]

Two principal problems occur in a practical implementation of Eq. (31): (i) Whether and under which conditions the (pseudo)inversion of the $X$-matrix exists. We have to deal with independent experimental conditions $x=1 \ldots M$, so that the $X$ matrix does not contain linearly dependent columns. (ii) How to determine $\widetilde{\mathrm{inv}}(X)$ experimentally? In principle, the $X$ matrix and its (pseudo)inversion can be calculated. But, in practice, the agreement between experiment and theory is not always sufficient. These two problems will be discussed below.

### B. Existence of the $\widetilde{\mathrm{inv}}(X)$ matrix

Considering the polar complex representation of the Kerr effect, $\Phi_x^{(i)} = \Omega_x^{(i)} \exp[i\xi_x^{(i)}]$, the definition of the Kerr signal $s_x^{(i)} = \Re\mathrm{e}[\Phi_x^{(i)} \exp(-i\psi_x)] = \Re\mathrm{e}[\Omega_x^{(i)} \exp(i\xi_x^{(i)} - i\psi_x)]$ [Eq. (4)] and of the depth sensitivity function $q_x^{\langle i,1 \rangle} = \Phi_x^{(i)}/\Phi_x^{(1)} = |q_x^{\langle i,1 \rangle}| \exp[i\Delta\xi_x^{\langle i,1 \rangle}]$ [Eq. (15)], the components of the $X$ matrix are expressed as

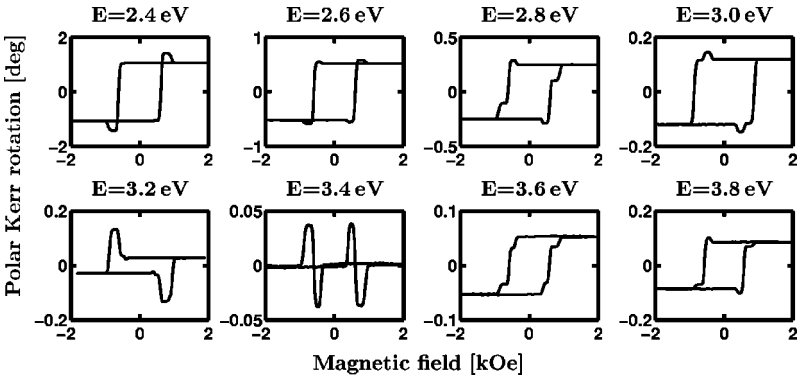


FIG. 12. Example of polar Kerr rotation hysteresis loops measured at several photon energies $E$ on the $(\mathrm{TbFe/Si_3N_4})_4$ sample. Each step in the hysteresis loop corresponds to a Kerr signal coming from a given TbFe stack.

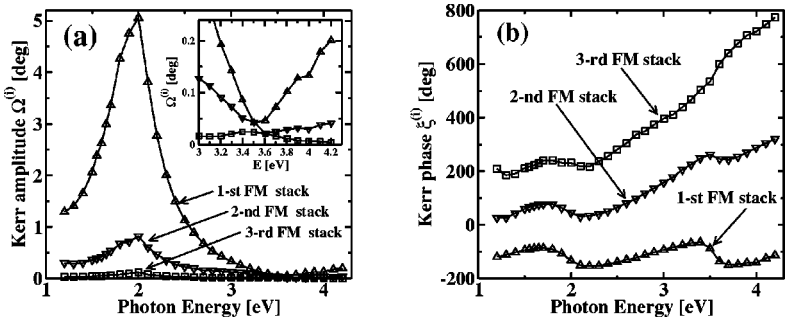


FIG. 13. Experimental Kerr effect spectra [(a) Kerr amplitude $\Omega^{(i)}$, (b) Kerr phase $\xi^{(i)}$] of each FM stack in the $(TbFe/Si_3N_4)_4$ system.

$$s_x^{(i)} = \Omega_x^{(1)} |q_x^{\langle i,1\rangle}| \sin(\xi_x^{(1)} + \Delta\xi_x^{\langle i,1\rangle} - \psi_x). \tag{32}$$

Now let us discuss the conditions under which the $X$ matrix has linearly independent columns. Because the term $\Omega_x^{(1)}$ is just a multiplicative constant of each $X$-matrix line, it does not play any role in the following discussion.

In the case of an $(M\times 2)$ $X$ matrix (for two FM layers), one only needs to have $\psi_1 \neq \psi_2$, $\xi_1^{(1)} \neq \xi_2^{(1)}$, or $q_1^{\langle i,1\rangle} \neq q_2^{\langle i,1\rangle}$. This is a sufficient condition for the existence of $\widetilde{\text{inv}}(X)$.

In the case of a $(M\times N)$ $X$ matrix; $N\geqslant 3$ (for three or more FM layers), the conditions of existence of $\widetilde{\text{inv}}(X)$ are not as straightforward as in the previous case, and it is shown that the depth sensitivity function $q$ has to vary with some parameters. Let us first consider the case of $M$ experimental configurations $(M\geqslant N)$, which differ only by the projection angle $\psi_k \neq \psi_l$, $(k\neq l)$ or in the Kerr phase of the first FM layer $\xi_k^{(1)} \neq \xi_l^{(1)}$, *keeping* depth sensitivity function $q_l^{\langle i,1\rangle} = q_k^{\langle i,1\rangle} = |q^{\langle i,j\rangle}| \exp[i\Delta\xi^{\langle i,1\rangle}]$ const. Then, the $\widetilde{\text{inv}}(X)$ is only possible if the matrix with components

$$\hat{s}_x^{(i)} = |q^{\langle i,1\rangle}| \sin(\xi_x^{(1)} + \Delta\xi^{\langle i,1\rangle} - \psi_x) \tag{33}$$

has linearly independent columns. Because the components $\psi_x$ and $\xi_x^{(1)}$ are the same for all terms in each line, and terms $|q^{\langle i,1\rangle}|$ and $\Delta\xi^{\langle i,1\rangle}$ are the same in all terms in each column, it can be shown that such a matrix (and consequently the $X$-matrix) *always* has linearly dependent columns.

Consequently, in the case of three or more FM layers, to select the Kerr signal coming from each FM layer it is not sufficient to perform MO experiments at different projection angles $\psi_x$. All Kerr vectors have to change independently, which is a situation that is not fulfilled if only $\Omega_x^{(1)}$ and $\xi_x^{(1)}$ are varied while keeping $q_x^{\langle i,1\rangle}$ constant. Hence it is necessary to choose such experimental conditions to give different depth sensitivity functions $q_x^{\langle i,1\rangle}$. In conclusion, for $N\geqslant 3$, different Kerr signals $s_x$ have to be measured at several photon energies or incidence angles, otherwise the $X$ matrix has linearly dependent columns.

### C. Inversion of the *X* matrix

In this subsection we discuss how Eq. (30), $\mathbf{s}^{(\text{tot})} = X\cdot\boldsymbol{\mu}$, can be solved if the elements of the $X$ matrix are not *a priori* known. In other words, we wish to find how to tune the linear combination of several $s_x^{(\text{tot})}$ to obtain a Kerr signal $s^{(i)}$ providing information about the magnetization state of a single FM layer in the multilayer structure. In principle, the $\widetilde{\text{inv}}(X)$ can be calculated theoretically; however due to the inaccuracy of optical and MO parameters, layer thicknesses and additional interface contributions, it can happen that the reliability of these calculations is not good enough.

The key idea of $\widetilde{\text{inv}}(X)$ tuning is a generalization of the numerical projection method introduced earlier for a two FM layers structure [Eq. (27)]: $s^{(\bar{i})} = s_1\cos\psi^{(\bar{i})} + s_2\sin\psi^{(\bar{i})}$, where $s_1$, $s_2$ are two different Kerr signals determined experimentally. For a given tuned projection angle $\psi^{(\bar{i})}$, one cancels the Kerr signal due to the $i$th FM layer, and consequently $s^{(\bar{i})}$ measures only the magnetization of the second FM layer. Applying this algorithm recursively, one can successively cancel Kerr signals from other FM layers. From an algebraic point of view, this algorithm is similar to the Gaussian elimination method.

This tuning procedure, based on a successive cancellation of signals from all layers in the multilayer structure, except for one, requires a knowledge of at least the approximate shape of hysteresis loops for individual layers. It is necessary to decide whether the observed hysteresis loop is a superposition of many contributions. This is quite easy in our simple case of square hysteresis loops with different coercive fields.

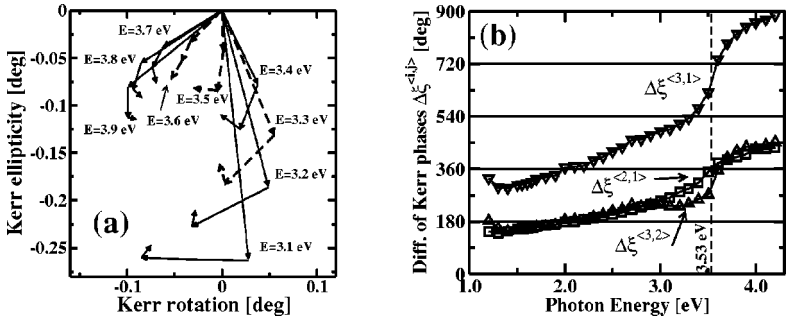


FIG. 14. (a) Experimental Kerr effect originating from each FM stack in the $(TbFe/Si_3N_4)_4$ system, for several photon energies. (b) Differences between Kerr phases $\Delta\xi^{(i,j)}$ as a function of the photon energy. If $\Delta\xi^{(i,j)} = n180°$, the $i$th and $j$th Kerr vectors are parallel.

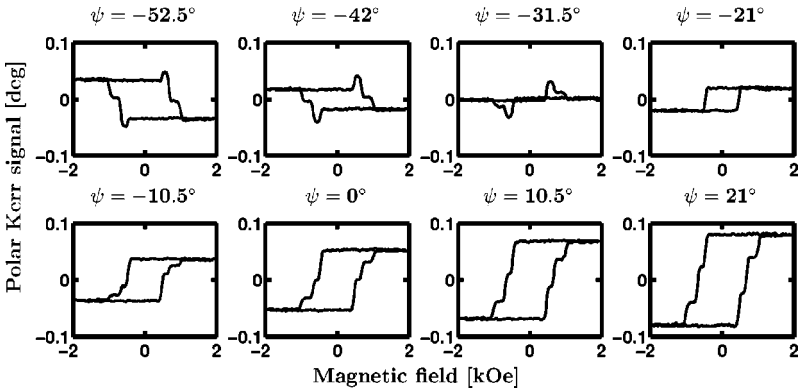


FIG. 15. Kerr hysteresis loops for several values of the projection angle $\psi$ and for the $(TbFe/Si_3N_4)_4$ system. The photon energy ($E=3.53$ eV) is chosen so that Kerr vectors $\Phi^{(1)}$ and $\Phi^{(2)}$ are parallel. Consequently, there is a projection angle $\psi$ (here $\psi=-21°$) for which the measured Kerr signal depends only on the magnetization state of the third FM layer.

For other hysteresis loop shapes this procedure is applicable as well. If the tuning procedure cannot be performed, the $\widetilde{\text{inv}}(X)$ matrix should be calculated theoretically with carefully selected optical and MO parameters of all layers. A combination of both methods is possible as well: approximate values of projection angles are calculated through Eq. (38) from the $X$ matrix, and afterward they can be finely tuned.

As an example of tuning procedure, let us take a three-FM-layer structure, on which three different Kerr signals $s_1^{(\text{tot})}$, $s_2^{(\text{tot})}$, and $s_3^{(\text{tot})}$ are measured. All these Kerr signals $s_i^{(\text{tot})}$ are different, and they are superpositions of Kerr signals originating from all three FM layers. As an example, let as show how to separate Kerr signals originating only from the first and second FM layers. Two independent projections between $s_1^{(\text{tot})}$, $s_2^{(\text{tot})}$ and between $s_1^{(\text{tot})}$ and $s_3^{(\text{tot})}$ can cancel the Kerr signal coming from the third FM layer,

$$s_{1,2}^{(\bar{3})}=s_1^{(\text{tot})}\cos\psi_{1,2}^{(\bar{3})}+s_2^{(\text{tot})}\sin\psi_{1,2}^{(\bar{3})}, \tag{34}$$

$$s_{1,3}^{(\bar{3})}=s_1^{(\text{tot})}\cos\psi_{1,3}^{(\bar{3})}+s_3^{(\text{tot})}\sin\psi_{1,3}^{(\bar{3})}, \tag{35}$$

and thus the Kerr signals $s_{1,2}^{(\bar{3})}$ and $s_{1,3}^{(\bar{3})}$ are different and depend only on effects coming from the first and second FM layers. Then we can once more apply the projection procedure to separate Kerr signals coming from the first or second FM layer:

$$s^{(1)}=s_{1,2}^{(\bar{3})}\cos\psi^{(1,\bar{3})}+s_{1,3}^{(\bar{3})}\sin\psi^{(1,\bar{3})} \tag{36}$$

$$s^{(2)}=s_{1,2}^{(\bar{3})}\cos\psi^{(2,\bar{3})}+s_{1,3}^{(\bar{3})}\sin\psi^{(2,\bar{3})}. \tag{37}$$

Hence, in a system composed of three FM layers ($N=3$, $M=3$), to be selective to only one FM layer one has to tune three projection angles $\psi$ subsequently. To deduce Kerr hysteresis loops of all three FM layers, seven projection angles have to be tuned. Similarly, for four FM layers ($N=4$, $M=4$), six projection angles have to be tuned to separate the Kerr signal coming from one FM layer. For separating Kerr hysteresis loops of all four FM layers, 16 projection angles are required.

If the Kerr signal values originating from the $i$th FM layer, $s_1^{(i)}$ and $s_2^{(i)}$, are known, the projection angle $\psi_{1,2}^{(\bar{i})}$, which cancels the Kerr signal of the $i$th FM layer, is [Eq. (27)]

$$\tan\psi_{1,2}^{(\bar{i})}=-\frac{s_1^{(i)}}{s_2^{(i)}}. \tag{38}$$

When values of $s_x^{(i)}$ are known, but not with sufficient accuracy, the derived values of $\psi^{(\bar{i})}$ can be used as starting points of the projection tuning.

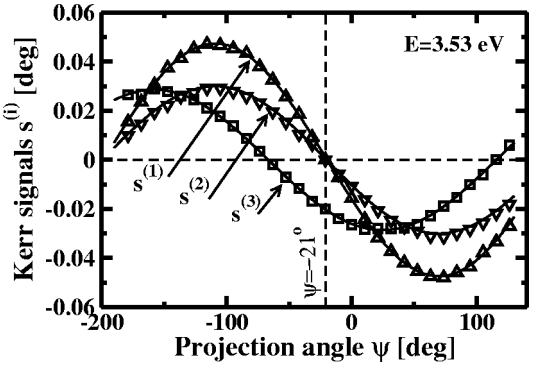


FIG. 16. Experimental variation of Kerr signals $s^{(i)}$, measured at $E=3.53$ eV, as a function of the projection angle $\psi$, for each FM stack in the $(TbFe/Si_3N_4)_4$ system. These curves were obtained from hysteresis loops presented in Fig. 15. For $\psi=-21°$, $s^{(1)}$ and $s^{(2)}$ cancel simultaneously and the Kerr signal measured at $E=3.53$ eV and $\psi=-21°$ comes only from the third FM stack. The full lines are sinusoidal fits.

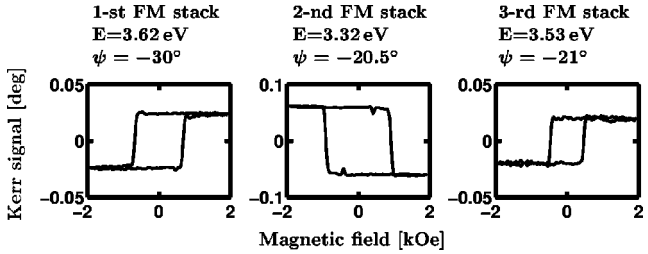


FIG. 17. Individual Kerr hysteresis loops deduced for each TbFe stack in the $(TbFe/Si_3N_4)_4$ system, obtained by choosing $E$ and $\psi$ to cancel Kerr effects of two TbFe stacks. Values of $E$, $\psi$ are indicated above each loop.

### D. "Cascade numerical projection" method applied to the $(Au/Co)_3$ film structure

The "cascade numerical projection" method allows one to separate the Kerr signal originating from each FM layer through linear combinations of several experimental Kerr signals, each consisting of a sum of contributions issued from different FM layers. It is based on a subsequent (i.e., cascade) numerical canceling of Kerr signals from an arbitrary FM layer, up to obtain a Kerr signal only related to the considered FM layer.

This technique is applied here to the Au(5 nm)/Co(0.6 nm)/Au(5 nm)/Co(1 nm)/Au(5 nm)/Co(1.4 nm)/Au(24 nm)/glass multilayer [Fig. 7(c)] already studied in Sec. III B. The sample preparation and characterization were described in Ref. 24. All Co layers displayed perpendicular magnetic anisotropy and provide square hysteresis loops. Since the Co layer thickness varies from layer to layer, the associated coercive field decreases when increasing the thickness.[25]

As discussed in Sec. VI B, Kerr signals have to be measured for at least two different values of the depth sensitivity function $q_x$. Hence we measured both Kerr rotation and ellipticity hysteresis loops at 2.5 and 3.8 eV. The measurements were performed at nearly normal incidence ($\varphi = 7°$, the measured *p*-Kerr effect) and the measured loops are presented on the left side of Fig. 18. The presented loop at 2.5 eV is measured for a projection angle $\psi = 33°$, but the particular value of this projection angle has no special meaning.

Each experimental loop is due to contributions of all three Co layers, resulting in three step loops. For a given linear combination of the two original loops one can cancel out the contribution from a given Co layer: $s = s_1 \cos\psi + s_2 \sin\psi$. The projection angle $\psi$ can be determined just by tuning the projection angle up to remove the Kerr signal coming from the targeted Co layer. By this first projection two loop hysteresis curves result depending only on Kerr signals coming from the first and third Co layers and two from the first and second Co layers (Fig. 18).

After this first projection, one has pairs of *different* Kerr hysteresis loops both depending, for example, on the magnetization of the first and the third Co layers. Hence the subsequent second projection can cancel out the Kerr signal coming from one more Co layer and the Kerr signal originating from only one Co layer may be separated (Fig. 18). Thus we succeeded in separating Kerr signals coming from each FM layer.

Let us comment on the decrease of the signal to noise ratio (SNR) at each projection stage. The noise amplitude of the projected Kerr signal is determined by the sum of the noise corresponding to each hysteresis loop. On the other hand, for each projection, the amplitude of Kerr signal itself is decreased. After the first projection shown in Fig. 18, the SNR is reduced by a factor of $2\sqrt{2}$. After the second projection, the SNR is reduced again approximately by a factor $10\sqrt{2}$. This large decrease of the SNR at this second stage is due to the close-to-one value of the depth sensitivity $q$. We estimate that the forthcoming projection will decrease the SNR approximately by a factor 5–10. The reduction of the SNR at each projection stage is more significant for thinner spacer layer. The SNR decreasing rate with the number of projections depends upon the linear independence of columns in the *X*-matrix [Eq. (30)], which is determined by the change of the depth sensitivity function $q_x$ corresponding to particular experimental conditions $x$.

### E. Volume magneto-optical recording for four storage layers

The question raised here is how to realize a convenient four-layer magneto-optical recording media by thin-film engineering. The properties of the $(FM/nFM)_4$ proposed structure are the following: (i) The MO readout can be done at a single photon energy. (ii) each FM layer is perpendicularly magnetized and exhibits a polar square hysteresis loop. (iii) The Kerr rotation signal carries information about the magnetization state of two FM layers and the Kerr ellipticity gives information about the magnetization state of the two other FM layers. (iv) The magnetization states of these two FM layers are distinguished by the so-called four-level MO readout procedure.[29,30] This means that FM layers provide Kerr signals with different amplitudes and, consequently, for two opposite magnetization states in each FM layer four Kerr levels are measured.

These conditions may be fulfilled if the four FM layers lead to the following Kerr vector configuration [Fig. 11(c)]: (i) Kerr vectors $\Phi^{(1)}$ and $\Phi^{(3)}$ and $\Phi^{(2)}$, $\Phi^{(4)}$ are mutually parallel. (ii) Kerr vectors $\Phi^{(1)}$, $\Phi^{(3)}$ are parallel to the Kerr rotation axis $\theta$, and $\Phi^{(2)}$ and $\Phi^{(4)}$ are parallel to the Kerr ellipticity axis $\epsilon$. In each pair of parallel Kerr vectors, one of them must be about two times larger than the other $(\Omega^{(1)}/\Omega^{(3)} \approx 2,\ \Omega^{(2)}/\Omega^{(4)} \approx 2)$. Thus the polar Kerr rotation (ellipticity) measurements provide four possible levels,

$$\theta = \Omega^{(1)} m_z^{(1)} + \Omega^{(3)} m_z^{(3)} = \{-\Omega^{(1)} - \Omega^{(3)}, -\Omega^{(1)} + \Omega^{(3)}, \Omega^{(1)} - \Omega^{(3)}, \Omega^{(1)} + \Omega^{(3)}\}, \tag{39}$$

$$\epsilon = \Omega^{(2)} m_z^{(2)} + \Omega^{(4)} m_z^{(4)} = \{-\Omega^{(2)} - \Omega^{(4)}, -\Omega^{(2)} + \Omega^{(4)}, \Omega^{(2)} - \Omega^{(4)}, \Omega^{(2)} + \Omega^{(4)}\}, \tag{40}$$

so that the magnetization state of each FM layer can be determined.

In conclusion, the readout of both the Kerr rotation and Kerr ellipticity at a *single* photon energy gives access to the magnetization state of all *four* buried FM layers. This solution combines the advantages of readout by both the Kerr rotation and ellipticity[30] and a four-level MO readout.[29]

## VII. CONCLUSION

In this paper, we have proposed ways to solve the general problem of how to determine the magnetization state of each FM layer in a multilayer structure by means of the magneto-optical Kerr effect.

First, the measured Kerr signal is interpreted as a projection of the Kerr effect in the complex $\theta\epsilon$-plane onto a projection axis fixed by the MO setup. The Kerr effect is ana-

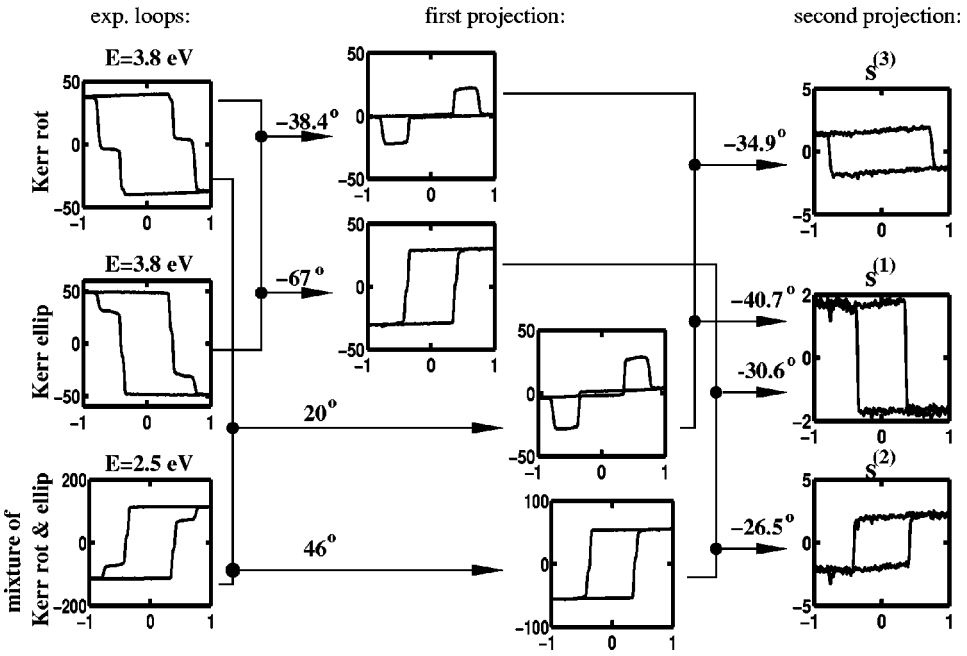


FIG. 18. Demonstration of the ''cascade numerical projection'' procedure for the $(Au/Co)_3$ sample. The three experimental hysteresis loops on the left side account for the magnetization state of all three Co layers. By two subsequent projections with angles $\psi$, the Kerr signal depending on the magnetization state of only one Co layer is separated. The numbers denote the projection angle $\psi$ values used for linear combination of given pair of hysteresis loops. The units of the Kerr signal and an external magnetic field and the Kerr signal are mdeg and kOe, respectively.

lytically expressed for each FM layer in the framework of the ultrathin film approximation. The depth sensitivity function $q$ is introduced and expressed analytically. This approach allows one to determine the variation between Kerr effects originating from FM layers located at different depths. Then we show, both theoretically and experimentally on simple model systems, how to straightforwardly determine the in-depth location of a FM layer if the saturated Kerr effect is known for each FM layer. A consistent approach is developed, providing a separation of Kerr signals coming from each FM layer in a FM bilayer structure, by a variation of the photon energy, the incidence angle, or the compensator phase shift. We show how to separate polar, longitudinal, and transverse components of the magnetization, in order to handle in-depth magnetometry measurements.

To be selective to the magnetization state of each FM layer, we propose and demonstrate the power of two different approaches: the ''parallel Kerr vector'' and ''cascade numerical projection'' methods. The ''parallel Kerr vector'' method is based on a tuning of some parameters (for example the photon energy and compensator phase shift). On the other hand, the ''cascade numerical projection'' allows one to separate Kerr signals originating from each individual FM layer by means of well-chosen linear combinations of Kerr hysteresis loops measured in different experimental conditions. For that purpose it is shown that Kerr hysteresis loops have to be measured for, at least, two different photon energies. Finally, we propose a suitable Kerr vectors configuration that can be realized in an engineered film structure for providing a volume magneto-optical recording solution in four storage layers.

## ACKNOWLEDGMENTS

One of the authors (J.H.) would like to thank the Laboratoire de Physique des Solides, Université Paris-XI, Orsay for its hospitality during his stays. M.N. would like to thank the Max Planck Institute of Microstructure Physics in Halle, Germany for its kind hospitality during his present stay. The financial support of J.H. on a the European Marie-Curie Grant No. HPMF-CT-2000-00066 and of the Ministère Français des Affaires Étrangères is greatly appreciated. This work was partially supported by the Grant Agency of the Czech Republic (Grants Nos. 202/00/0761 and 202/99/D060). The authors wish to thank A. Mougin for critical reading of the manuscript.

*Corresponding author: Email address: hamrle@karlov.mff.cuni.cz
†Present address: Max-Planck-Institut für Mikrostrukturphysik, Weinberg 2, D-06120 Halle, Germany.

[1] S. Bader and J. Erskine, in *Ultrathin Magnetic Structures II*, edited by B. Heinrich and J. Bland (Springer-Verlag, Heidelberg, 1994), p. 297.
[2] J. Ferré, in *Magnetism and Synchrotron Radiation*, edited by E. Beaurepaire, F. Scheurer, G. Krill, and J.-P. Kappler (Springer, Berlin, 2001), p. 316.
[3] M. Rührig, R. Schäfer, A. Hubert, R. Mosler, J. Wolf, S. Demokritov, and P. Grünberg, Phys. Status Solidi A **125**, 635 (1991).
[4] R. Schäfer, J. Magn. Magn. Mater. **148**, 226 (1995).
[5] A. Hubert and G. Traeger, J. Magn. Magn. Mater. **124**, 185 (1993).
[6] V. Kamberský, L. Wenzel, and A. Hubert, J. Magn. Magn. Mater. **189**, 149 (1998).
[7] G. Pénissard, P. Meyer, J. Ferré, and D. Renard, J. Magn. Magn. Mater. **146**, 55 (1995).
[8] M. Pufall, C. Platt, and A. Berger, J. Appl. Phys. **85**, 4818 (1999).
[9] J. Ferré, P. Meyer, M. Nývlt, Š. Višňovský, and D. Renard, J. Magn. Magn. Mater. **165**, 92 (1997).
[10] J. Ankner and G. Felcher, J. Magn. Magn. Mater. **200**, 741 (1999).

[11] R. Nakajima, J. Stöhn, and Y. U. Idzenda, Phys. Rev. B **59**, 6421, (1999).
[12] F. Nolting, A. Scholl, J. Stöhr, J. Seo, J. Fompeyrine, H. Siegwart, J.-P. Locquet, S. Anders, J. Luning, E. Fullerton, M. Toney, M. Scheinfein, and H. Padmore, Nature (London) **405**, 767 (2000).
[13] M. Bonfim, G. Ghiringhelli, F. Montaigne, S. Pizzini, N. Brookes, F. Petroff, J. Vogel, J. Camarero, and A. Fontaine, Phys. Rev. Lett. **86**, 3646 (2001).
[14] F. Sirotti, S. Girlando, P. Prieto, L. Floreano, G. Panaccione, and G. Rossi, Phys. Rev. B **61**, R9221 (2000).
[15] R. Osgood III;, S. Bader, B. Clemens, R. White, and H. Matsuyama, J. Magn. Magn. Mater. **182**, 297 (1998).
[16] A. Hubert and R. Schäfer, *Magnetic Domains: The Analysis of Magnetic Microstructures* (Springer-Verlag, Berlin, 1998).
[17] K. Sato, J. Phys. Soc. Jpn. **43**, 719 (1977).
[18] R. Azzam and N. Bashara, *Ellipsometry and Polarized Light* (North-Holland, Amsterdam, 1992).
[19] G. Traeger, L. Wenzel, and A. Hubert, Phys. Status Solidi A **131**, 201 (1992).
[20] Š. Višňovský, M. Nývlt, V. Prosser, R. Lopušník, R. Urban, J. Ferré, G. Pénissard, D. Renard, and R. Krishnan, Phys. Rev. B **52**, 1090 (1995).
[21] Š. Višňovský, Czech. J. Phys. **48**, 1083 (1998).
[22] Z. Qiu and S. Bader, J. Magn. Magn. Mater. **200**, 664 (1999).
[23] H. Ding, S. Pütter, H. Oepen, and J. Kirschner, Phys. Rev. B **63**, 134425 (2001).
[24] J. Hamrle, M. Nývlt, Š. Višňovský, R. Urban, P. Beauvillain, R. Mégy, J. Ferré, L. Polerecký, and D. Renard, Phys. Rev. B **64**, 155405 (2001).
[25] V. Grolier, Ph.D. thesis, Orsay, Paris, 1994.
[26] K. Nakagawa and A. Itoh, J. Magn. Soc. Jpn. **20**, 73 (1996).
[27] M. Nývlt, J. Ferré, J. Jamet, P. Houdy, P. Boher, Š. Višňovský, R. Urban, and R. Lopušník, J. Magn. Magn. Mater. **156**, 175 (1996).
[28] J. Pommier, J. Jamet, J. Ferré, P. Houdy, P. Boher, and F. Pierre, J. Magn. Magn. Mater. **136**, 251 (1994).
[29] N. Saito, R. Sato, N. Kawamura, and M. Kajiura, Jpn. J. Appl. Phys. **28**, 343 (1989).
[30] K. Nakagawa, A. Itoh, K. Shimazaki, M. Yoshihiro, and N. Ohta, J. Magn. Soc. Jpn. **23**, 221 (1999).
[31] W. Press, S. Teukolsky, W. Vetterling, and B. Flannery, *Numerical Recipes in C: The Art of Scientific Computing* (Cambridge University Press, Cambridge, 1992).